Title

MICROSTRUCTURAL AND MAGNETIC CHARACTERIZATION IN SOFT MAGNETIC FE-SI-AL (SENDUST) ALLOY

Author

Kim, J.D.

Publication Date

1988-12-01

Lawrence Berkeley Laboratory
UNIVERSITY OF CALIFORNIA

Materials & Chemical Sciences Division

Microstructural and Magnetic Characterization in Soft Magnetic Fe-Si-Al (Sendust) Alloy

J.D. Kim
(Ph.D. Thesis)

December 1988

Prepared for the U.S. Department of Energy under Contract Number DE-AC03-76SF00098.

DISCLAIMER

LBL-26334

Microstructural and Magnetic Characterization in Soft Magnetic Fe-Si-Al (Sendust) Alloy

J.D. Kim
(Ph.D. Thesis)

Department of Materials Science and Mineral Engineering
University of California
and
Materials and Chemical Sciences Division
Lawrence Berkeley Laboratory
1 Cyclotron Road
Berkeley, California 94720

December 1988

MICROSTRUCTURAL AND MAGNETIC CHARACTERIZATION IN SOFT MAGNETIC FE-SI-AL SENDUST ALLOY

JUNE DONG KIM

Ph.D

Department of Materials Science and Mineral Engineering

Sponsor: U. S. Department of Energy
Daewoo Electronics Co., Ltd.

Abstract

Microstructure and its effect on magnetic domain structure and domain wall motion has been studied to understand the role of microstructure in determining the magnetic properties of a soft magnetic Sendust alloy. Electron microscopy of dark field imaging utilizing superlattice reflections has been mainly used to investigate the ordering behavior and corresponding microstructural changes, and Lorentz electron microscopy allowed the effect of microstructure on magnetic domain structure and wall motion to be observed. Antiphase boundaries (APBs) and other imperfections have been shown clearly and simultaneously with the observation of magnetic domain walls, even with the

objective lens off.

It was shown that the ordering phase transitions in an $Fe_3Si_{0.6}Al_{0.4}$ Sendust alloy follows the same sequence, namely α->B2->DO_3 as that in binary iron-silicon and iron-aluminium alloys. The B2->DO_3 phase transition commenced on cooling below 1,030°C and followed a nucleation and growth process, developing a two-phase region. The two phase region existed down to at least 900°C. Although the phase transition could not be suppressed by quenching, the two-phase region could be identified by the existence of interfacial dislocations in quenched specimens.

The microstructure at room temperature consisted of single phase DO_3. However, as-quenched microstructures from the two-phase region showed interfacial superlattice dislocations bound with APBs. These superlattice dislocations have the Burgers vector of 1/2<100> type, consistent with their being misfit interfacial dislocations. APBs could be shown as dark bands of contrast in superlattice reflections and showed no apparent preference for any particular crystallographic plane. The displacement vector of APBs was shown to be 1/2<100>.

The magnetic domain structures of the alloy in the remanent state after saturation revealed closure domains at the edge of the specimen and at cracks. Closure domains were also observed at grain boundaries, inclusions and holes. From in-situ studies of domain wall motion it was shown that the

interactions of domain walls with individual dislocations and APBs are not sufficiently strong to be observed, as domain walls passed straight across them. However, grain boundaries act as strong pinning sites for domain walls, and closure domains formed at holes leading to a retardation of the domain wall motion.

Grain boundaries are shown to be the most detrimental structural defects for soft magnetic applications of the Sendust alloy. Therefore, they should preferably be removed by suitable heat treatment. For this purpose, it might be desirable to anneal the material in the single phase region to facilitate large grains but to avoid any interfacial dislocations which would be formed at interphase interfaces in the two phase field. The presence of inclusions and holes is also likely to be undesirable for soft magnetic applications of the Sendust alloy. Suggestions for improving Sendust for recording heads are therefore to have clean, non-porous alloys of very large grain size, preferably single crystal.

MICROSTRUCTURAL AND MAGNETIC CHARACTERIZATION IN SOFT MAGNETIC FE-SI-AL SENDUST ALLOY

CONTENTS

I. General Introduction

The aim of this research is to understand the relationship between microstructure and magnetic properties in soft magnetic Sendust alloys for their application to magnetic recording head.

In recent years, there has been increasing interest and correspondingly significant research in the area of magnetic recording technology, which includes recording heads and storage media as well as recording processes. The basic processes of magnetic recording are depicted in figure 1 [1]. The recording head and the storage medium (disk or tape) are in a state of motion with respect to each other. The field generating current in the coil creates a magnetic field which emanates from the gap region of the head and magnetizes a small region of the ferromagnetic medium (writing or recording). The recorded wavelength (λ) is related to the frequency (f) of the field generating current and the velocity (v) of the moving medium as $\lambda = v/f$. The recorded information can be recovered at a later point in time using the reading feature of the head. The flux lines that radiate from the magnetized regions on the surface of the storage medium induce a voltage in the head windings. The voltage is proportional to the number of turns and the rate of flux change [1,2].

Recording heads have been fabricated from materials which

are magnetically soft and are characterized by high saturation magnetization, high permeability, low coercivity, and low remanent magnetization. Specifically, high saturation magnetization is required for writing performance so as to transfer the input signals to the storage media without saturation of head pole tips, and high permeability is required for reading performance so as to pick up the recorded signals effectively. Currently there are three main types of materials for recording heads. For general-purpose audio recording, the recording medium is γ-Fe_2O_3, with a coercivity of about 240 A/cm (300 Oe). In this case the head material is usually laminated Permalloy, sometimes precipitation-hardened through the use of alloying elements to reduce head wear. For high-quality audio and video recording the medium is CrO_2 or cobalt-impregnated γ-Fe_2O_3, with a coercivity of about 480 A/cm (600 Oe). Here both Sendust and spinel ferrites are used as head materials [3].

Recently, the trend toward high recording density has led to the need for high coercivity recording media and high operating frequencies. Metallic recording particles with a coercivity of 1200 A/cm (1500 Oe) are now available, and the design frequency is up to 10 MHz. As the wavelength or the bit length of the recorded signals becomes shorter, demagnetizing fields become larger and must be resisted by higher coercivities [3,4]. In this case material requirements for recording heads are becoming more severe. Shibaya et al.

[5] showed experimentally that the saturation magnetization of head cores should be about five times the coercivity of media to produce beneficial effects in short wavelength recordings. In addition, high electrical resistivity of head cores is required to reduce the eddy current loss. No single known material has this combination of properties. Ferrites have extremely high electrical resistivity and wear resistance but low saturation magnetization, whereas metallic materials such as Sendust and Permalloy have high saturation magnetization but low electrical resistivity [3].

Interest in further developing Sendust alloy as a promising head material for high density recording stems primarily from its high saturation magnetization ($Ms \approx 10^4$ Gauss) as well as high permeability ($\mu_i \geq 10^4$) and good wear and corrosion resistance [6,7]. Yasuda et al. [8] first examined the writing and reading efficiencies of the Sendust and ferrite head for media with coercivities of 700-1700 Oe, and showed that the writing efficiency of the Sendust head is superior to that of the ferrite one, especially for higher coercivity media because of its high saturation magnetization, while the reading efficiencies of both heads are comparable. Furthermore, in spite of its low electrical resistivity, below the thickness of 15 μm, the effective permeability and the loss factor of the Sendust head become comparable to those of manganese-zinc ferrite head even at frequencies above 5 MHz [7].

However, it is very difficult to produce recording head cores from a bulk Sendust material because it is mechanically so hard and brittle. For this reason its use has been limited to low frequency applications in bulk configuration and high frequency inductors in powder core form [9]. Processing has therefore been a prime consideration. Much work has been carried out and several head designs have been suggested, utilizing sputtering and roll quenching techniques. Two of them commonly known are the ferrite/Sendust composite head named metal-in-gap (MIG) head [10-13] and the sandwich-type head [14,15]. The MIG head is a ring head with Sendust sputtered on either one or both sides of inner-gap pole faces made of ferrites, and in the sandwich-type head, the Sendust core is laminated by ferrites in the direction of track width.

The magnetic properties that play important roles in the application of soft magnetic materials can be divided into intrinsic or structure-insensitive, and extrinsic or structure-sensitive properties. Saturation magnetization is one of structure-insensitive properties, while permeability and coercive force are structure-sensitive properties [16]. Early studies showed that high permeability in the Sendust alloy is closely connected with very small values of magnetocrystalline anisotropy (K_1) and magnetostriction constant (λ) [17-19]. Subsequently, it was shown that the permeability as well as the coercivity are very sensitive to

heat treatment conditions, especially annealing temperature and quenching temperature following annealing [20-23]. Furthermore, it was shown that the sign and the magnitude of K_1 and λ change drastically by a small change of alloy concentration and also temperature, and that the compositions at which K_1 and λ become zero are strongly temperature-dependent [24-29].

From the structural point of view, Sendust alloy is located close to the composition line which connects 25 at.% silicon-iron (Fe_3Si) with 25 at.% aluminum-iron (Fe_3Al) [20]. Thus, the existence of the ordered structures, B2 and DO_3, should be taken into account when discussing the soft magnetic properties of this alloy.

The magnetic properties of crystallographically ordered materials are usually found to be strongly dependent on the presence of crystal defects and these properties can therefore be affected by heat treatment [30-32]. The defects present in materials can alter the magnetic domain structure, or exert forces on domain walls. It has been well established from earlier investigations on ferromagnetic materials with ordered structures such as iron-silicon [31], iron-aluminum [30], copper-manganese-aluminum [32,33], etc., that the magnetic properties can be changed over a wide range by modifying the microstructure. From these studies, the optimum microstructures have been obtained for each alloy. However, no such studies have been carried out on the Sendust alloy,

and the optimum condition for heat treatment has not been established.

The objectives of this research are thus two fold: first, to characterize microstructure as a function of temperature and secondly, to investigate the interaction between magnetic domain walls and microstructure, with the hope of gaining a better fundamental understanding of the relationship between microstructure and properties in order to guide further processing development.

II. Microstructural Characterization

1. Introduction

Sendust is an iron-base alloy containing 8-11 wt.% Si and 4-8 wt.% Al [17,34]. This composition is close to the stoichiometric composition of $Fe_3(Si,Al)$ [20]. Early X-ray work suggested the existence of the ordered B2 and DO_3 phases in the Sendust alloy, based on iron-silicon and iron-aluminum alloys [21,35]. However, since then little has been known about the microstructure, and still an iron-silicon-aluminum ternary phase diagram has not been established.

To study the microstructure of the ordered alloy, the distinction between first order and second order transition is worth making because the microstructures and transformation kinetics in the two cases are different [36]. For example, first order transitions progress isothermally by a process of nucleation and growth, whereas second order transitions occur homogeneously throughout the material.

The microstructure in an $Fe_3Si_{0.6}Al_{0.4}$ Sendust alloy has been investigated by utilizing transmission electron microscopy (TEM). This work consisted of the observation of ordering behaviour and corresponding microstructural changes. Dark field imaging in the electron microscope using superlattice reflections can provide information concerning the critical ordering temperature and the nature of an

ordering transition which is both more accurate and easier to interpret than that obtained by more traditional techniques such as X-ray diffraction, specific heat measurement and neutron diffraction [37,38].

2. Background

2.1 Ordering behavior in iron-aluminum and iron-silicon binary alloys

Figure 2a [39-42] shows the phase diagram for iron-aluminum alloy system, which was drawn from data obtained in observations by TEM of the microstructures found in quenched specimens. This phase diagram displays that there are two ordered phases, B2* (FeAl) and DO_3* (Fe_3Al), and the transitions of α (disordered bcc) -> B2 and B2 -> DO_3 are of second order for appropriate alloys. The line of second order transitions for the disordered α -> B2 transition ends in a symmetrical tricritical point, and below this point the transition is of first order [43,44].

Figure 2b [38] shows the phase diagram of iron-silicon alloy system. This was first constructed by Swann et al.,

---

* Strukturbericht (Structure Report) notation

combining their experimental results with the theoretical calculation by Inden et al. [45]. Inden et al. calculated configurational free energies for the ordering sequence of disordered α -> B2 -> DO_3 as a function of temperature and composition in terms of order parameters and the first nearest neighbor and second nearest neighbor interchange energies for the reaction 2FeSi = FeFe + SiSi, and predicted the ranges of stability of these phases over a wide range of composition and temperature. This was shown as a solid line in figure 2b. The symbols in figure 2b show the phases observed experimentally at the temperatures and compositions indicated.

It can be seen that no two-phase regions are present, except for the B2 + DO_3 region below the critical temperature. All other transitions are of second order, one phase changing homogeneously into another without the development of a two-phase mixture.

The above two phase diagrams differ in a number of ways: (1) the ordering transitions at any particular temperature occur at higher alloy contents in the iron-aluminium alloys, (2) the B2 and DO_3 ordering temperatures are much lower in iron-aluminum alloys, (3) the B2 ordering transition is both of first and second order in iron-aluminium alloys but only of second order in iron-silicon alloys. Most of these differences can be explained qualitatively in terms of the smaller first nearest and second nearest neighbor interchange

energies in iron-aluminum alloys [38]; they are approximately half those of iron-silicon alloys [46,47].

2.2 B2 and DO_3 superlattice

The unit cell of the B2 superlattice is shown in figure 3a, where the atom sites are divided into equal numbers of sublattices labeled I and II. In the state of perfect long range order, all of the sites associated with one sublattice are occupied by either all A or all B atoms. Therefore, each B atom has all A atoms for first nearest neighbors and vice versa. For instance, in Fe_3Al alloys, iron atoms occupy the sublattice II, while I is occupied by a random distribution of the remaining iron and aluminum atoms, so that the ordered arrangement is actually an imperfect CsCl type [48,49].

A superlattice type closely related to the B2 type is the DO_3 structure, the unit cell of which is shown in figure 3b. In the DO_3 structure, the lattice can be subdivided into four interpenetrating fcc sublattices, where A atoms occupy atom sites on sublattices II, III and IV, while the remaining B atoms occupy type I sublattice sites. In Fe_3Al alloys, iron atoms occupy A sites and aluminum atoms occupy B sites. The lattice parameter is twice that of the corresponding disordered bcc alloy, and the most characteristic feature of this DO_3 structure is that the atoms are arranged such that the maximum number of first unlike as well as second unlike

nearest neighbor pairs are formed, which means the aluminum atoms are arranged in such a manner that they avoid having aluminum atoms as either first or second nearest neighbors [48].

2.3 Antiphase domain structure

In the B2 structure, displacements of the atoms in a 1/2<111> direction produce first nearest neighbor stacking errors or antiphase boundaries (APBs). On the other hand, there are two types of APB that can be produced in the DO_3 structure, i.e., two different antiphase vectors. The first type is formed by a displacement of B atoms located on I sites onto either II or IV sites in figure 3b. In this case, the antiphase vector is a $1/4a_o'$<111> type and this boundary includes only like first nearest neighbor pairs. Note that if the antiphase vector were to be expressed in terms of a_o shown in figure 3a, then it would be $1/2a_o$ [111], or exactly the same as for the B2 superlattice. The second distinct type of APB is formed by a displacement of B atoms from I site to III site. The antiphase vector is a $1/2a_o'$<010> type and this type of displacement does not result in like first nearest neighbor atom pairs across the APB, but leads to like second nearest neighbor atom pairs [48].

These antiphase boundaries are either formed thermally during the ordering transformation or associated with

dislocations [49,50]. As the ordering transformation proceeds first by the nucleation of small ordered regions, a particular atom species within a given nucleus will very often choose a specific sublattice which is different from that chosen by the same atom species in a neighboring nucleus. When the nuclei grow and they eventually come into contact, the interface between the two different ordered domains will consist of an APB, which is called a thermal APB [49].

APBs can also be formed by the slip motion of dislocations [50]. The ordered lattice has a lower symmetry than the corresponding disordered lattice from which it transformed. Furthermore, the periodicity of the lattice along certain crystallographic directions is increased over that of the corresponding disordered alloy. If this increase in periodicity occurs along the slip direction, then it follows that dislocations which were perfect in the disordered alloy, will not be perfect in the ordered alloy. In particular, the dislocations, if they were to move through the superlattice, would in most cases be required to leave behind them a ribbon of disorder across the slip plane, the so-called slip-produced APB. In general, an APB formed by an imperfect dislocation will have an antiphase vector identical to that of the Burgers vector of the dislocation from which it was formed [48].

The paired dislocations bound by APBs are called

superlattice dislocations, which are able to move through a superlattice without creating any net change in order across the slip plane. The dislocations which constitute the superlattice dislocation exert a mutual repulsive force upon each other that is balanced by the surface tension of APBs. The equilibrium extension of the superlattice dislocation can be found by the interaction energies between the dislocations and the APB energies [50-53].

2.4 Contrast mechanism for revealing APBs by TEM

All of the atoms on one side of the APB are out of phase with respect to those atoms on the other side of the boundary. Therefore, APBs can be imaged by interference contrast which results from the phase difference between waves scattered on opposite sides of the boundary. The contrast mechanism for revealing APBs has been discussed by treating it as a stacking fault [49,54-57].

When a foil is oriented so that the electron beam is incident at a Bragg angle, then the diffracted intensity I_D varies periodically within the foil. The foil is assumed to be critically oriented so that only one beam with indices hkl corresponding to the reciprocal lattice vector $\mathbf{g}$ is diffracted at the Bragg angle θ. Since the intensity associated with the incident wave I_I must be conserved, then to a good approximation (neglecting absorption and

simultaneous excitations)

$$I_I = I_D + I_T,$$

where I_T is the intensity associated with the transmitted wave. The incident wave is diffracted completely at a distance $t_o/2$ within the foil, where t_o is the extinction distance.

When a planar fault is present within a foil, a wave crossing the fault may suffer a phase change $e^{i\alpha}$. The phase angle α may be expressed by

$$\alpha = 2\pi \mathbf{g}\cdot\mathbf{p},$$

where $\mathbf{g}$ is the reciprocal lattice vector associated with a particular reflection hkl and $\mathbf{p}$ is the displacement vector associated with the fault. As a consequence, the diffracted intensity is modified in the faulted region resulting in periodic variations in intensity proportional to t_o, and perpendicular to the fault.

The specific values of α clearly depend on the specific structures concerned. For the structure considered here, only the possible values for α for DO_3 (figure 3b) are listed in Table 1, since the B2 phase is never observed. There are two possible types of APBs in the DO_3 superlattice, i.e., 1/4<111> and 1/2<100>. It can be seen that α turns out always to be an integral multiple of 2π when $\mathbf{g}$ corresponds to a fundamental reflection, but can be equal to an odd multiple or fraction of π when $\mathbf{g}$ corresponds to a superlattice reflection. Thus for an APB inclined to the plane of the

film, fringe contrast characteristic of the phase shift due to the boundary is obtained when certain superlattice reflections are operating.

APB contrast will consist of alternately light and dark equally spaced interference fringes parallel to the boundary. The spacing between successive light or dark fringes is proportional to the extinction distance and the extinction distance is given by the following relation:

$$t_o = \pi a_o^3 \cos\theta / \lambda F,$$

where λ is the wavelength of the electrons, θ is the Bragg angle, and F is the structure factor associated with the particular crystal lattice and reflection. It is apparant that since the extinction distance is inversely proportional to the structure factor, the extinction distances for superlattice reflections are quite large compared to those for fundamental reflections. This is because the structure factor for fundamental reflections is equal to the sum of the individual atomic scattering factors for the alloy while the structure factor for superlattice reflections varys as their difference, and is therefore smaller than that for fundamental reflections [48,49].

3. Experimental

The alloy with the composition of Fe-9.34 wt.% Si-5.34 wt.% Al (approximately $Fe_3Si_{0.6}Al_{0.4}$) was prepared by vacuum induction melting, using electrolytic iron (99.9%), silicon (98.5%) and electrolytic aluminum (99.99%) as starting materials. The ingot was homogenized at 1200°C for 5 hours in an Ar atmosphere.

Specimens for heat treatments were prepared by cutting and mechanical grinding to a thickness of 0.25mm. They were heat-treated in two ways in a vertical tube furnace in air. First, to determine the phase transition temperature roughly, specimens were held for 1 hour at the temperature range of 900°C to 1,200°C, and then quenched into iced brine (figure 4a). Secondly, to investigate the microstructural changes produced during the phase transition, specimens were held for 1/2 hour at 1,100°C, furnace-cooled to specific quenching temperatures, held for 1 to 24 hours, and then quenched into iced brine (figure 4b). The temperature was controlled to an accuracy of ±2°C.

Transmission electron microscopy (TEM) has been used to investigate the microstructure in quenched specimens. Thin foils for TEM observation were prepared by electro-jet polishing in a mixture of perchloric acid 15% and acetic acid 85% at 10V and ~13°C. Electron microscopy was performed using a Philips EM 301 microscope operating at 100 kV.

4. Results

The main effect associated with the atomic ordering is a modification in diffraction patterns due to a change in the structure of the unit cell [58]. As it was already described in Section 2.2, the ordered B2 and DO_3 phases have a simple cubic and a face centered cubic Bravais lattice, respectively. In the B2 structure all hkl reflections are possible, while in the DO_3 structure only reflections with unmixed indices are allowed. Therefore, the disordered bcc, B2 and DO_3 phases can be recognized by structure factor contrast in dark field micrographs. Table 2 [38] summarizes these intensities for various operating reflections. In order to positively identify the structure of two-phase ordered alloys two dark-field images are required using reflections with indices which sum to an odd integer and twice an odd integer, respectively. It should be noted that all the indices are referred to the axes of the large DO_3 unit cell shown in figure 3b, and, typically the 111 and 200 (or 222) reflections are chosen since these have the highest intensities.

Figures 5a and b, respectively, show dark field micrographs taken of the 111 superlattice reflection in an as-cast specimen and in a specimen held for 1 hour at 1032°C and then quenched into iced brine. Figure 5c shows a tableau of selected area diffraction patterns (SADPs) from both

specimens. The 111 and 311 reflections are clearly seen, and these must be superlattice reflections. Therefore, these SADPs are exactly the same as those for the fcc structure. This indicates that both specimens consisted of single DO_3 ordered domains. The uniform bright contrast from the ordered domains in figure 5b corresponds with the expected dark field structure factor contrast in Table 2. The quenched specimen consists of much smaller DO_3 domains than the as-cast specimen. Taking into account this difference in domain size, it can be deduced that the phase transition takes place below 1,032 °C, and cannot be suppressed by quenching.

APBs are clearly shown as dark bands of contrast, not in fringe contrast, in figure 5b, which agrees with the findings of Fisher and Marcinkowski [55]. However, the APB in figure 5a exhibits a single pair of white fringes, and a solid gray and white band contrast. This might be due to slight change in orientation of the foil from the exact Bragg angle. In thick regions of the foil that are oriented very near to the Bragg angle, subsidiary fringes of equal intensity and spacing of half an extinction distance appear at APBs and this produces such pair of fringes [49]. In addition, the contrast reversal from dark to white occurs quite frequently due to the large extinction distance, which makes the periodic variation of the boundary contrast very sensitive to small changes in orientation [48].

Identification of APBs in quenched specimens was

performed and an example is given in figure 6. APBs are clearly seen in the 111 superlattice reflection (figure 6a), but the boundary contrast vanishes in the 200 superlattice reflection (figure 6b). These contrast data show that the APB has a displacement vector of 1/2<100> type.

An interesting microstructure is shown in figure 7. These are dark field micrographs taken in a specimen quenched from 1,025°C. The 111 superlattice reflection shows a different morphology of APBs (figure 7a) and the 222 superlattice reflection reveals dislocations at which APBs are terminated (figure 7b). The matrix phase consists of a single phase DO_3 with large domain size and thus the quenching temperature is below the phase transition temperature.

Figures 8, 9 and 10 show microstructures from step quenching experiments to further determine the transition temperature and to investigate microstructural changes which occur during the phase transition. A difference is shown in microstructures above and below the transition temperature. From the quenching temperature of 1,030°C, the microstructure consists of only small ordered DO_3 domains having 1/2<100> type APBs (figure 8), while microstructures from the quenching temperature of 1,026°C show dislocations delineating characteristic morphologies such as a boundary (figure 9) and a second phase particle (figure 10), in which fundamental reflections of 220 type revealed the dislocation contrast and superlattice reflections of 111 type revealed

the associated APB contrast. Microstructures from the quenching temperature of 1,024°C show the same dislocation morphologies in figures 11 and 12, but in this case the matrix phase consists of large DO_3 ordered domains, unlike that in figures 9 and 10.

The difference in domain size of the matrix phase indicates that the phase transition which occurs on cooling below 1,030°C is the B2 -> DO_3 phase transition. The previous B2 matrix phase in figures 8, 9 and 10 was transformed to the DO_3 phase during quenching, and thus the resulting matrix phase consists of small DO_3 domains. The dislocations in figure 9 may be interfacial dislocations formed at the interface of the B2 and DO_3 phases, suggesting that small regions of the DO_3 nucleate along the APB of the former B2 phase. Figure 11 shows the growth of such DO_3 nuclei at the expense of the B2 phase.

The prior existence of the B2 phase is clearly shown in figure 12. The morphology of the former B2 phase was further analyzed in figures 13 and 14. The complex configuration shown in figure 13a is actually a fingerprint of where B2 transformed to DO_3 leaving behind interfacial superlattice dislocations each connected by APBs (faintly visible in figure 13b). The Burgers vector of these interfacial dislocations is shown to be 1/2<100> type in figure 14, which is consistent with their being misfit B2/DO_3 interfacial dislocations. At the quenching temperature, the atomic

displacements in the 1/2<100> direction do not produce APBs because they are not the antiphase vector in the B2 phase. But during cooling when the B2 phase transforms to the DO_3 phase, APBs form, and also the phase boundary between the DO_3 and the former B2 phase disappears. Therefore, the microstructure at room temperature shows only a fingerprint of the interfacial superlattice dislocations connected by APBs (figure 13c).

The B2 phase exists down to the quenching temperature of 900°C. Figures 15a and b show microstructures in specimens quenched from 960°C and 900°C, respectively, and show the decrease in domain size of the former B2 phase with decrease in quenching temperature.

Here it is noted that the boundary contrast vanishes along the line of intersection of two APBs associated with interfacial dislocations in figure 15. It was already shown in figure 13a that the boundary contrast also vanishes at the points of intersection of APBs associated with dislocations and thermally produced APBs. This contrast behavior of APBs can be understood by the fact that the phase factor α associated with the superlattice reflections, giving rise to the contrast of 1/2<100> type APB, is $\pm\pi$, which is shown in Table 2, and the two intersecting APBs produce a total phase change of $\pm 2\pi$ in the diffracted electrons, and thus give rise to no modification in their intensity. However, according to Marcinkowski [49], this simple cancellation of the phase

factor α can occur only in the case that two APBs are quite likely parallel and very close each other over their common region of overlap. As the two APBs become spaced further apart, the individual phase contrasts may be resolved.

Another interesting microstructural feature is that microstructures in specimens annealed at 1,100°C show interfacial dislocations such as those shown in figure 11, which formed along the APB of the B2 phase (figure 16a). The density of these dislocations depends on holding time at the annealing temperature. Further experiments showed that those dislocations exist in specimens annealed at 1,045°C and higher (figure 16b), while there are no dislocations formed in specimens annealed at 1,040°C and below (figure 16c). It was previously shown that there are no dislocations formed in specimens annealed at around 1,030°C (figure 5b), possibly indicating a B2 single phase region. Therefore, the interfacial dislocations shown in figures 16a and b might be related to another two phase region, i.e., disordered α + B2 phase field.

Summary: On the basis of the above explanations, it can be deduced that the phase transition in an $Fe_3Si_{0.6}Al_{0.4}$ Sendust alloy follows the same sequence, viz., disordered α -> B2 -> DO_3 as that in iron-silicon and iron-aluminium alloys. However, the disordered α -> B2 and B2 -> DO_3 transition occurs in a nucleation and growth process, developing a two-phase region. Although the phase transition

could not be suppressed by quenching, the two phase region could be identified by the existence of interfacial dislocations in quenched specimens and the phase boundary between B2 and DO_3 could be determined from the difference between their DO_3 domain sizes on quenching.

5. Discussion

5.1 Ordering behaviour

Order-disorder phase transitions are thermodynamically classified into two types, according to the lowest derivative of the free energy which changes discontinuously at the critical temperature. If this discontinuity occurs in the first derivative, the transition is described as the first order phase change, which in ordered alloys corresponds to a discontinuous change in the average compositions of the sublattices of the ordered structure at the critical temperature. In first order phase transitions, as the chemical potential is varied, the relative amounts of the two phases change while the temperature remains constant. The phase diagram for such transitions thus contains two-phase regions in which the "lever rule" for the relative amounts of each phase is obeyed. This is in contrast to the second order transitions which change sublattice compositions continuously with temperature and which can occur without the appearance of the usual two-phase region [37,42,57]. Therefore, the observation by TEM of equilibrium two-phase microstructures constitutes a sensitive method for distinguishing between first and second order phase transitions.

On the other hand, in alloys undergoing second order phase transitions the change in free energy corresponding to

a certain change in the degree of order becomes vanishingly small as the transition temperature is approached so that strong, localized fluctuations in the degree of order are expected near the transition temperature [38]. Such fluctuations have been observed directly by TEM in iron-silicon [38] and iron-aluminum [37] specimens quenched from the neighborhood of the transition temperature.

However, in the present investigation no such fluctuations have been observed and this evidence together with the observation of the two-phase fields deduced from the existence of the interfacial superlattice dislocations can positively identify the first order phase change of the disordered α -> B2 and B2 -> DO_3 in a Sendust alloy.

Theoretically, the order of order-disorder transitions has been predicted by the Landau theory [59,60]. The theory provides a number of criteria which must be satisfied in order for a transition to be of the second order. These criteria are: 1) The space group of the symmetry elements of the ordered structure must be a subgroup of the space group of the disordered solid solution. 2) The ordering wave vectors must be located at the "special points" of the reciprocal lattice of the disordered phase. 3) It must be impossible to find three members of the star of ordering wave vectors which will sum up to a reciprocal lattice vector. A star of a vector is a set of vectors which can all be derived from one single vector by applying all the symmetry

operations of the lattice. From these criteria, the disordered α -> B2 and B2 -> DO_3 transitions can be of both first and second order, while the α -> DO_3 transition must be of first order. Recently Sluiter et al. [61] confirmed this by the Cluster Variation Method (CVM) in the tetrahedron approximation in the calculation of order-disorder transitions on the bcc lattice.

In view of the ordering behaviour in the Sendust alloy, this is the first systematic experimental study by TEM. The result is in good agreement with the above theoretical prediction but not with the previous X-ray diffraction work by Chang [62] and Takahashi et al. [63]. They suggested that in the Sendust alloy with the stoichiometric composition, the disordered α phase transform directly to the DO_3 phase without forming the B2 phase, and that this transition is of second order, which is not consistent with the Landau theory, without any conclusive evidence. However, in the present investigation, the interfacial dislocations shown in figures 11, 16a and b reflect the prior existence of B2-type APBs and consequently the prior existence of the B2 phase. This indicates that the ordering sequence is disordered α -> B2 -> DO_3, instead of disordered α -> DO_3. The ordering sequence of α -> B2 -> DO_3 has also been observed directly by hot-stage TEM in iron-20 at.% aluminum-5 at.% silicon alloy [64].

5.2 Microstructure

During the ordering process, the atomic rearrangements in the disordered bcc structure produce the simple cubic structure of the B2 phase and further the fcc structure of the DO_3 phase. The unit cell of the DO_3 phase consists of eight unit cells of the B2 phase and the edge length is usually expressed as twice that of the B2 phase.

However, there might be a lattice mismatch at the interface of the B2 and DO_3 phase in the two phase field due to the difference in crystal structure and composition. Table 3 summarizes nearest neighbor atomic arrangements in the B2 and DO_3 phase with the stoichiometric composition of $Fe_3(Si,Al)$. It can be seen that there are differences in second nearest neighbor atoms. This difference in second nearest neighbor atoms combined with the difference in composition may contribute to the slight difference in lattice parameters of the B2 and the DO_3 phase in the two phase region. In the DO_3 structure, the silicon and aluminium atoms do not have silicon and aluminium atoms in either first or second nearest neighbors, and this indicates that in the DO_3 structure, the second nearest neighbor energy is relatively large [48]. From the measurements of the transition temperatures of α -> B2 and B2 -> DO_3 it has been reported that the second nearest neighbor energy in iron-silicon and iron-aluminum alloys is approximately half

the first nearest neighbor energy [45,47]. The Burgers vector of 1/2<100> type of dislocations in specimens quenched from the two phase region suggests that they are misfit interfacial dislocations.

The difference in lattice parameters between the B2 and DO_3 phase has been observed in the two phase region of iron-silicon alloys [38]. On the DO_3-rich side of the B2 + DO_3 phase field below the Curie temperature, the B2 phase is present as a thin layer on the DO_3 domain boundaries, and this B2 phase could be observed by an asymmetrical δ-fringe contrast (strain contrast) which results from the slight difference between lattice parameters of the B2 boundary layer and the DO_3 matrix. This strain contrast has also been observed within the "K-state" region in iron-aluminum alloys by Warlimont and Thomas [65] and they suggested that it is due to the difference between lattice parameters of the disordered α and DO_3 phase. In addition, the strain contrast and further interfacial dislocations, depending on the size of second phase particles, have been observed when disordered hexagonal phases exist on domain boundaries of ordered hexagonal DO_{19}-type phases in titanium-aluminum alloys [66].

On the other hand, the characteristic microstructure in long-range ordered alloys is the antiphase domain structure, which consists of APBs. There are two types of APBs in the DO_3 phase and the corresponding antiphase domain structure will consist of 1/2<100> type APBs surrounded by 1/4<111>

type APBs [43,48,50]. This can be analyzed by considering the atomic rearrangements which occur during ordering, referring to the sublattice sites of the DO_3 unit cell shown in figure 3b.

On cooling below the critical temperature, the B2 phase forms from the disordered bcc structure by the ordering of first nearest neighbour atoms and the DO_3 phase forms by the further ordering of second nearest neighbour atoms [38]. In the B2 phase, sites of type I and III, and II and IV are equivalent, and the I and III sites are occupied by iron atoms and the II and IV sites are occupied by the remaining iron, silicon and aluminum atoms. During the course of the B2 -> DO_3 phase transition, the iron, silicon and aluminum atoms that were previously arranged at random on the II and IV sites take positions such that type II sites are occupied by silicon and aluminum atoms while the remaining IV sites are occupied by iron atoms. Therefore, in the DO_3 phase these sites are no longer equivalent, and the nuclei of the DO_3 phase will be characterized within each domain of the B2 phase. APBs in the B2 phase have an antiphase vector of 1/2<111> type, and within these APBs, as small DO_3 domains come into contact during growth, APBs with the antiphase vector of a 1/2<100> type will form. Since the B2-type APB is structurally equivalent to the 1/4<111> APB in the DO_3 phase, then the antiphase domain structure in the DO_3 phase must consist of 1/2<100> type APBs surrounded by 1/4<111> type

APBs [48,50].

In the present investigation, the 1/4<111> type APBs delineated from the interfacial dislocations show very nearly straight line traces and indicate very large domains, and the 1/2<100> type APBs show no apparant preference for any particular crystallographic plane. The smoothly curved APB configuration shown in figure 6a indicates a low, isotropic APB energy, and this has been accounted for by the relatively small energy difference between the APBs lying in different planes in this alloy [67,68].

III. Magnetic Characterization

1. Introduction

The observation of magnetic domains and the investigation of the effect of microstructure on magnetic domain structure and wall motion is a key element in the characterization of a magnetic material. It provides qualitative information about the effect of microstructure on the magnetic properties and has led to the development of various processing techniques so as to optimize the microstructural variables for the desired combination of properties [69,70].

Lorentz electron microscopy (LEM) enables the defects and magnetic domain structures to be imaged simultaneously, and is therefore capable of giving detailed information about their interactions [71]. The strength and direction of the magnetic field in the plane of the specimen can be controlled by appropriately tilting and rotating the specimen so that it is at an angle with the magnetic flux of the objective lens, and correspondingly the dynamics of the domain wall motion and its interaction with the microstructures can be examined directly. Since the domain wall motion is related to many of the magnetic properties, such dynamic studies are of interest in understanding the magnetic behavior of the materials.

The main disadvantage of this technique is the necessity of using very thin specimens. In many materials, the

interactions between individual defects and domain walls are not sufficiently strong to be observed in thin foils. Neverthless, such observations can provide qualitative information in relation to the interaction of microstructural features and domain walls [30].

In this section, a LEM study of magnetic domain structures and the effect of microstructure on the magnetic domain structures and the wall motion is described. The motion of the domain wall is studied in situ.

2. Domain structure and magnetization process (background)

2.1 Magnetic domains

Ferromagnetic materials are characterized by spontaneous magnetization below the Curie temperature. However, the magnetization curve asserts that an unmagnetized ferromagnetic sample displays no overall magnetization in zero field even below the Curie temperature. This leads directly to the question of how an assemblage of spontaneously magnetic atoms can be demagnetized [16,72,73].

This problem was resolved by postulating that a bulk sample is subdivided into many different regions, called domains, in the demagnetized state. Within each domain, all

the atomic moments are aligned in one of the easy directions; therefore, spontaneous magnetization does exist. The direction of spontaneous magnetization, however, varies from domain to domain so as to minimize the magnetostatic energy. On a purely statistical basis, all available easy directions will be used equally in the material. Hence the specimen as a whole will not show a net magnetization in the absence of an applied field [72-74].

2.2 Bloch walls

Bloch walls are domain boundaries, which are interfaces between regions in which spontaneous magnetization has different directions. The change of spin direction between domains magnetized in different directions takes place in a gradual way over many atomic planes. The reason for the gradual nature of the change is the fact that, for a given total change of spin direction, the exchange energy is lower when the change is distributed over many spins than when the change occurs abruptly. On the other hand, the spins within the wall are pointing in noneasy directions, so that the crystal anisotropy energy within the wall is higher than it is in the adjoining domains. While the exchange energy tries to make the wall as wide as possible, in order to make the angle between adjacent spins as small as possible, the anisotropy energy tries to make the wall thin, in order to

reduce the number of spins pointing in noneasy directions. Therefore, the competing effect of these two energies gives rise to an equilibrium wall width at which the sum of these two energies is minimum [2,73].

There are characteristic crystallographic planes in which the domain wall lies. The choice of the wall surface is not so wide and random because it tends to meet the condition that no free poles are created at the wall. This condition is satisfied if the components of magnetization parallel to the wall are completely cancelled and the components of magnetization normal to the wall are either completely cancelled or continuous [16].

2.3 Domain structure

In the absence of an external field, magnetocrystalline anisotropy forces tend to align the domain magnetization in one of a number of preferred directions. Moreover these domains must form so that the effects of demagnetizing fields arising from the free poles are small. The demagnetizing fields are produced either at a boundary between adjacent domains or at the surface of a specimen where there is a change in the normal component of the magnetization [75].

The avoidance of free poles at a boundary between adjacent domains is the guiding principle controlling the orientation of domain walls. For example, a 180° domain wall

must be parallel to the magnetization vectors in the adjacent domains. Otherwise, free poles will form on the wall, creating magnetostatic energy. For the same reason, a 90° wall must lie at 45° to the adjoining magnetization vectors [2].

The demagnetizing field from the specimen surface can be reduced by dividing domains into smaller domains. However, the extent of the sub-division is limited by the presence of boundary walls between adjacent domains, with which there is a finite energy associated. Equilibrium is reached when the reduction in magnetostatic energy brought about by any further sub-division is offset by an increase in boundary energy associated with the increased wall area [2,73,75].

The formation of closure domains near the surface of the specimen reduces the formation of free poles still further. The possible arrangement of closure domains below a surface perpendicular to one crystal axis was first suggested by Kennard [76]. In closure domains, the component of magnetization normal to the boundary is continuous across the boundary, and no poles are formed anywhere in the crystal. The flux circuit is completed within the crystal, and the magnetostatic energy is therefore reduced to zero. Note that a closure domain structure should have the magnetization parallel to the surface at all free surfaces [2,75,76].

In closure domain structures, the domain size is determined by a balance between the effects of Bloch wall

energy and magnetostrictive energy. The closure domains are magnetized perpendicular to the primary domains and this introduces an elastic strain energy term into the total energy. This term is called the magnetostrictive energy, and is directly proportional to the square of the magnetostriction constant, the elastic modulus and the total volume of the closure domains. The total closure domain volume can be reduced by making the primary domains smaller. Therefore, the magnetoelastic energy tends to make the domains small, while the Bloch wall energy tends to make the domains large. The equilibrium domain configuration is the result of minimizing the sum of these two energy terms [2,72].

As described above, usually the flux closure configuration has a lower energy than the simple slab configuration. However, with increasing values of the ratio K/Ms^2 the domains of closure gradually open up and for $1 \ll K/Ms^2$ the simple slab arrangement prevails [73]. Here K is the magnetocrystalline anisotropy constant and Ms the saturation magnetization.

2.4 Magnetization process

The process of magnetization under an applied magnetic field takes place on the domain theory by two independent processes: by an increase in the volume of domains which are

favorably oriented with respect to the field at the expense of unfavorably oriented domains; or by rotation of the directions of magnetization towards the direction of the field. In weak fields the magnetization changes often proceed by means of domain boundary displacements, so that the domains change in size. In strong fields the magnetization usually changes by means of rotation of the direction of magnetization in a fixed volume [73,74].

For instance, consider a single crystal of iron in the form of a square sheet with two (001) faces shown in figure 17 [16]. In the demagnetized state, there are four triangular domains of equal volume, of which two are spontaneously magnetized in the ±[100] directions and the other two magnetized in the ±[010] directions. Since the magnetization in every direction is counter-balanced, the crystal would not exhibit a net magnetization.

Now let a magnetic field be applied at a moderate angle, say 10°, from [010], as shown in figure 17b. Because this field direction is closer to [010] than any other <100> directions, the [010] domain will expand at the expense of the other three domains. Figure 17b shows that the expansion is affected by the movement of the boundaries between domains. In the early stage, the movement of domain boundaries usually is reversible; that is, the boundaries will tend to move back toward the original position when the field is reduced. However, crystals always contain

imperfections, such as impurities, dislocations, etc., which may act as barriers to the movement of domain boundaries. Thus, in the later stage, the movement of domain boundaries becomes non-uniform (figure 17c) and jerky, because only those segments of boundaries that have acquired enough energy from the field can overcome the barriers and continue the movement until new barriers are encountered. The movements of domain walls become irreversible after the initial stage, and the jerky style of the movements gives rise to the Barkhausen effect.

As the field is increased still further the atomic spins begin to rotate in two modes. One is the sudden 90° turning or 180° reversal of the spins in the $\pm$[100] or [010] domains into the [010] direction (figure 17d). This mode of rotation will eliminate all but the [010] domains. Consequently the entire crystal will have only one domain because all spins are now aligned in the [010] direction. The second mode of rotation involves the gradual turning of the spins from [010] to the direction of the field. The crystal eventually attains saturation magnetization when all spins have rotated into the field direction, as shown in figure 17e. The spin rotation in either mode is reversible.

3. Lorentz Electron Microscopy

3.1 Fresnel imaging (principle)

Lorentz electron microscopy (LEM) utilizes the deflection of the electron beam caused by direct interaction of the electrons with the magnetization of a thin film specimen as the electrons pass through it [77-79]. This deflection is due to the Lorentz force, which inevitably acts on any moving charged particle. The deflections are usually so small ($\sim 10^{-4}$ radian) and less than one tenth of a typical Bragg angle [80]. Such a small deflection will only have a slight effect on the standard in-focus image, being effectively equivalent to a small change in the incident beam direction or to a very small tilt of the specimen. Neverthless it is sufficiently large for significant contrast effects to be detected [80-82].

Magnetic domain boundaries separate regions of a ferromagnetic material that are magnetized in different directions. For simplicity, consider a foil with 180° domains in which the magnetization is parallel to the plane of the foil and the domain wall, and in opposite directions in alternate domains. The path of the electron beam is illustrated schematically in figure 18 [81,82]. The electron beam will be deflected in opposite directions in adjacent domains, leading to a deficiency of electrons at A and an

excess of electrons due to overlap at B. Therefore, if the foil is observed out of focus in the plane AB, the domain boundary will be imaged because of the local increase and decrease of intensity. This is known as the Fresnel imaging (out-of-focus) technique.

The domain walls will be revealed by black (excess) or white (deficiency) lines, and the finite width of these boundary images depends on the amount of defocusing and foil thickness. The contrast of the wall image is reversed when going from overfocus to underfocus of the objective lens and vice versa. The contrast reversal is readily explained by reference to figure 18. Overfocus is the condition of increased current of the objective lens such that its first focal plane is moved below the in-focus plane. Underfocus is the condition of reduced current of the objective lens such that its first focal plane is now moved above the in-focus plane. Since the specimen and the first focal plane of the objective lens are almost coincident for the in-focus condition, the first focal plane is below the specimen for overfocus and above the specimen for underfocus [83]. Therefore, for the overfocused condition, a convergent wall (A) will appear as a bright line and a divergent wall (B) as a dark line, and vice versa for the underfocused condition.

3.2 Experimental

In the normal operation mode of TEM, the specimen is immersed in a high magnetic field (~5 KGauss) due to the objective lens current in the vicinity of the specimen. Under this circumstance, for materials of low magnetocrystalline anisotropy and low coercivity such as Sendust, it is impossible for any domain walls to survive. It is therefore necessary to withdraw the specimen out of this magnetic field to a lower field.

For this purpose, in the present experiment, a Philips EM 301 microscope operating at 100kv has been used with the objective lens turned off and at low magnification (LM). In LM (100X - 4,000X) the Lorentz image can be focused with the diffraction lens. The projector lens current is fixed and the magnification is varied by changing the current through the intermediate lens [84]. A magnetic field can be applied to the specimen by exciting the objective lens with a very low current [84], and the direction and the strength of the magnetic field can be changed by tilting the specimen, and thereby the domain wall motion could be investigated. In order to obtain sharp domain wall images the incident beam should be as parallel as possible; consequently the condenser system is defocused to give effectively a point source a long way from the specimen [82,85].

4 Results and Discussion

4.1 Domain structure

Before describing the results of the present investigation, it is noted that since the specimens were first exposed to the objective lens current to investigate the microstructure, domain structures observed subsequently represent the remanent state after saturation.

The characteristic features apparent for all of the wall images observed are very nearly straight line traces and indicate very large domains. As one example, a pair of Lorentz images in both overfocused and underfocused conditions are shown in figure 19. The domain walls are shown clearly as a white and a dark line and the contrast is reversed when going from overfocus to underfocus. The width of domain walls increases with an increase in specimen thickness as shown in figure 20, and it also depends on the amount of defocusing.

It may be noted at C in figure 21 that occasionally the domain walls appear to end in the center of the specimen. The disappearance of the domain wall occurred in both the overfocused and the underfocused images. It is possible that this represented a widening of the domain wall so that the magnetization as a whole rotates [86]. Figure 22 is a schematic diagram of the magnetization distribution in this

interpretation. This is not unreasonable for a material of low magnetocrystalline anisotropy [73].

The domain structure at the edge of the specimen reveals closure domains, which are shown in figure 23. Closure domains have also been observed around a crack in figure 24. The assumed direction of the magnetization in each domain is indicated by arrows. This is based on the fact that in Lorentz microscopy black and white walls denote a change in the direction of the magnetization clockwise and counterclockwise, respectively [87].

It seems likely that in thin foils the magnetization is constrained to lie in the plane of the foil, because a huge demagnetizing field would act normal to the plane of the foil if the magnetization turned in that direction [88]. In this case domains extend completely through the foil thickness and the domain structure is governed mainly by the influence of the free poles at the edge of the specimen, so that closure domains form to reduce the magnetostatic energy. The energy required to form the closure domain comes mainly from the magnetocrystalline anisotropy. However, The directions of easy magnetization are the cube edges in bcc crystals, so that the direction of magnetization in the domains of closure can be in an easy direction at the same time that the magnetization in the basic slab-like domains is in another easy direction. This indicates that there is no energy contribution from the crystalline anisotropy and the closure

domain configuration is particularly stable in bcc crystals [73].

On the other hand, domain walls observed in these investigations are mainly of the 180° kind and might be of Bloch type. Cross-tie walls have also been observed in figure 24 and appear to be similar to those observed in Permalloy thin films [89]. In Bloch walls, which are found in bulk materials, the magnetization lies in the plane of the wall, so that the magnetostatic energy comes from free poles of the specimen surface. When the specimen thickness is small, the magnetostatic energy of the wall can be reduced if the spins in the wall rotate, not about the wall normal, but about the specimen normal. The result is a Neel wall. Free poles are then formed on the wall surface [2]. Cross-tie walls consist of a special kind of Neel wall, crossed at regular intervals by Neel wall segments, and they exist in the thickness range intermediate between Bloch and Neel walls [90].

The formation of the cross-tie wall can be understood by reference to figure 25a, which shows a Neel wall, separating two oppositely magnetized domains. It is not a normal Neel wall because it consists of segments of opposite polarity; these have formed in an attempt to mix the north and south poles on the wall surface more intimately and thus reduce magnetostatic energy. The regions within the wall where the polarity changes, marked with small circles, and where the magnetization is normal to the film surface, are called Bloch

lines. However, this hypothetical wall would have very large energy, because the fields due to the poles on the wall, sometimes called stray fields, are antiparallel to the domain magnetization in the regions opposite the Bloch lines marked A. As a result, spike walls form in these regions, as shown in figure 25b, and the stray fields close in a clockwise direction between the cross ties [2,75].

4.2 Domain walls/defects interaction

The presence of APBs and dislocations appears not to affect the domain wall configuration, and the domain wall passes straight across them. Figures 26 and 27 show domain walls intersecting APBs and regions of high dislocation density, respectively. The resolution of APBs and dislocations is necessarily weak due to the imaging conditions required to observe the magnetic domain. The motion of the domain walls has also been observed by specimen tilting with the objective lens off. Domain walls are seen to move successively through APBs and interfacial dislocations, delineating the former B2 phase, without any deflection (figure 28).

However, at a grain boundary, there is a closure domain formed, and during the course of dynamic observations a domain wall was pinned along the grain boundary. Small deflection in the direction of the domain wall is also

observed. A pair of Lorentz images in both overfocused and underfocused conditions in each stage of magnetization are shown in figures 29, 30 and 31. With the objective lens off, the domain wall A shows a closure domain C at the boundary, and the domain wall B is restricted in one of two grains (figure 29). When a small magnetic field is applied to the specimen by exciting the objective lens with a very low current, the closure domain in A disappeared and some parts in B crossed over the grain boundary and others was pinned by the grain boundary (figure 30). Further specimen tilting made domain walls move in the direction of the arrow and a new closure domain was created at C', and more parts of the domain wall B was pinned at the boundary (figure 31). The reference mark D indicates that the micrographs are from the same area.

The formation of the closure domain at the grain boundary is due to a discontinuity in the magnetization vector component normal to the boundary [2,91]. The grain boundaries in a polycrystalline specimen separate regions of different crystallographic orientation or easy magnetization direction. At low field strengths, the magnetization vectors of the neighboring grains are not rotated from their easy magnetization directions into complete alignment. Consequently, there is generally a discontinuity across the boundaries in the magnetization vector component normal to the boundary. Therefore magnetic poles exist at the grain

boundaries, and magnetic energy is associated with these poles. The presence of impurity atoms and inclusions at a grain boundary will enhance the effect, and cause reverse domains to form to reduce the number of free poles [16].

Another interesting interaction between a domain wall and a hole is shown in figure 32. A hole is a region where the material has a small enclosed free surface. The magnetization near a hole will be disturbed due to the formation of free poles at the hole [92]. As a result reverse domains formed in such a way that no free poles exist at the free surfaces.

The retardation of the wall motion around a hole was observed by specimen tilting with the objective lens off. This is shown in figure 33 with a sketch of the domain wall configuration. As a domain wall approached the hole H, a new domain formed between the moving wall and the hole, and this caused the moving wall to be bulged in the opposite direction to the wall movement (figure 33b). As the wall was forced to move further, it suddenly jumped as a result of magnetization reversal by rotation in the region between the hole and the impeded wall, and intersected the hole. It is noted that, however, in this case, reverse domains were not observed when the domain wall intersected the hole.

Magnetocrystalline anisotropy is the most effective means of impeding magnetization reversal by rotation processes. It provides an energy barrier resisting departure from the easy direction of magnetization that impedes the rotation process.

However, it has been known that the magnetocrystalline anisotropy is very small (nearly zero) in the Sendust alloy, and therefore, the retardation of the domain wall by a new domain around a hole was not observed to be significant.

Reverse domains are also nucleated at an inclusion. Free poles on the surface of a non-magnetic inclusion cause the formation of reverse domains so as to reduce the magnetostatic energy when a domain wall bisects the inclusion [73]. This kind of reverse domains was observed in figure 34.

IV. Summary of Results

The phase transition in an $Fe_3Si_{0.6}Al_{0.4}$ Sendust alloy follows the same sequence, viz., disordered α -> B2 -> DO_3 as that found in iron-silicon and iron-aluminium alloys. The B2 -> DO_3 phase transition commenced on cooling below 1,030°C and followed a nucleation and growth process, developing a two-phase region, which existed down to 900°C. Although the phase transition could not be suppressed by quenching, the two-phase region could be identified by the existence of interfacial dislocations in quenched specimens.

The microstructure at room temperature consisted of single phase DO_3. However, as-quenched microstructures from the two phase region showed interfacial superlattice dislocations bound with APBs. These superlattice dislocations have the Burgers vector of 1/2<100> type, consistent with their being misfit interfacial dislocations. APBs were resolved by imaging in superlattice reflections and showed no apparant preference for any particular crystallographic plane. These APBs were shown to be 1/2<100>.

Magnetic domain structures in the remanent state after saturation revealed closure domains at the edge of the specimen and cracks. Closure domains were also observed at grain boundaries, inclusions and holes due to the demagnetizing fields at these inhomogeneities. From in-situ studies of the domain wall motion it was shown that any

interactions of domain walls with individual dislocations and APBs are not sufficiently strong to be observed, since domain walls passed straight across them. However, grain boundaries act as strong pinning sites for domain walls, and closure domains formed at holes which lead to a retardation of domain wall motion.

V. Discussion

This study represents the first attempt at a detailed investigation of microstructure and its relation to domain walls in a Sendust alloy. In this section a discussion is given of the possible influence of microstructure on the magnetic properties.

The coercive force and the initial permeability are two important structure-sensitive magnetic properties for recording head application, that is, they may change in value by large amounts as a result of small changes in the metallurgical treatment [16]. Therefore, the recognition of the effect of microstructure on the coercive force and initial permeability can lead to the development of various processing techniques so as to optimize the microstructural variables for the desired combination of properties.

The coercive force in magnetically soft materials is usually very low due to low magnetocrystalline anisotropy and low magnetostriction, and may be determined by pinning-controlled mechanism [73]. In this case, the coercive force represents the field strength needed to carry a wall from one potential energy valley to another potential energy valley, past the highest intervening energy hump, while the initial permeability is determined by the field strength through which a domain wall may move without passing over a peak. Therefore, both of them are determined by essentially the

same physical conditions, and there is a very close correlation between them, materials with high coercivities having low permeabilities, and vice versa.

As it was indicated by the observation of a jerky motion of a domain wall, the energy of the specimen will vary in a more or less irregular way with the position of a domain boundary, as a result of local variations in internal strains, impurities, etc. In the absence of an applied magnetic field, the boundary will take up positions of minimum energy. The walls may be displaced from these positions by the application of a magnetic field, which in effect exerts a pressure on a wall tending to displace it so as to increase the magnetization in the direction of the field [2,73,74]. Therefore, the pinning of domain walls at defect structures is due to a local decrease in the energy of the specimen around those regions.

The domain wall has a definite surface energy which depends on the material and the nature of the boundary. The decrease in the specimen energy around defect structures has been first understood in terms of a reduction of the wall energy [2,73,89]. The presence of defect structures decreases the area, and hence the energy, of the wall, when a wall passes from outside the defects to a position bisecting them. Therefore, the domain wall has a strong tendency to stick to the defects. In this case, the pinning effect depends on the width of the domain wall. For large magnetocrystalline

anisotropy, the wall energy is high and walls become very thin, and even point defects may contribute to pinning. Planar defects with weakened exchange resulting from structural or chemical changes in the boundary region, such as grain boundaries, provide particularly effective pinning.

On the other hand, a later analysis by Neel suggested that, when a wall moves from a position away from defects to a position bisecting them, there is an energy reduction by the free-pole effect and this is much greater than the energy reduction by the wall-area effect [2,73,89]. For instance, an inclusion entirely within a domain would have free poles on it and there is an associated magnetostatic energy. The free pole distribution on the surface of the inclusion will be determined by the direction of magnetization in the domain wall. When the wall moves to the position bisecting the inclusion, the free poles are redistributed as shown in figure 35 [73], and the magnetostatic energy is approximately halved.

Neel further predicted the formation of closure domains at an inclusion which further reduced the magnetostatic energy [93]. The formation of such domains is dependent on the size of the inclusion. Usually it has been known that closure domains form only if the width of an inclusion is greater than the domain wall thickness [94]. When closure domains exist about inclusions, they retard domain walls which move past them with a force proportional to their

domain wall surface tension [95].

Qualitatively, this picture of the coercive process explains the fact that the coercive force diminishes and the initial permeability increases as the amount of inclusions and holes decreases and also as the grain size increases through annealing.

On the other hand, it has been known that the stress fields associated with dislocations interact importantly with magnetic domain walls [96,97]. This effect has its origin in the magnetoelastic coupling between the stress field and magnetostriction. In other words, a dislocation lying within a domain is the source of extra energy, mainly magnetoelastic, the amount depending on the relative orientation of the dislocation and the magnetization vector of the domain. If the stress field of the dislocation rotates nearby spins out of the easy direction by an appreciable amount, extra exchange and magnetostatic energy, which is due to the divergence of the magnetization, will be created. Therefore, although any significant interaction of domain walls with individual dislocation was not observed, the existence of dislocations might affect soft magnetic properties detrimentally. As one example, Seeger [96] showed that the coercivity is proportional to the square root of the dislocation density, while the initial permeability is inversely proportional to it. The interaction of domain walls with dislocations is confined to those lying inside the wall.

If a dislocation intersects a 180° wall, there is no interaction, in the sense that the wall can move with respect to the dislocation without any change in the energy of the system [86,96].

Silcox [86] suggested that the interaction of domain walls with individual dislocations in ferromagnetic materials might not be observed by Lorentz electron microscopy. The interaction is governed by the value of $(\lambda sGb)/(KA)^{1/2}$, where λs is the saturation magnetostriction, G the shear modulus, b the Burgers vector, K the magnetocrystalline anisotropy constant and A is the exchange constant. The term of $(KA)^{1/2}$ determines the wall energy, and its small value gives high wall energy and makes the wall thin. For a high pinning effect, the value of $(\lambda sGb)/(KA)^{1/2}$ should be high, and, of the common ferromagnetic metals, nickel has the largest value of this parameter. However, nickel does not show any pinning of the domain wall by dislocations, so that none of the other ferromagnetic materials is not expected to show such an effect.

In contrast to dislocations, APBs have been observed to interact very strongly with domain walls and tend to act as pinning sites for domain walls in alloys containing manganese, particularly in the manganese-aluminum alloy [98] and copper-manganese-aluminum Heusler alloy [33]. This pinning effect of APBs has been explained by assuming that the magnetic moments of manganese atoms on opposite sides of

APBs were coupled antiferromagnetically, so that the APB became an extremely narrow 180° domain wall [32,33,99].

The ordered DO_3 structure existed in the Sendust alloy is closely related to the $L2_1$ structure of the copper-manganese-aluminum alloy, and contains APBs with similar crystallographic properties to those present in the copper-manganese-aluminum alloy [48]. However, there was no significant interaction observed in this investigation and also previously in iron-aluminum alloys [32,100]. This indicates that there might be no antiferromagnetic coupling across APBs of these alloys and this absence of antiferromagnetic coupling might be due to the fact that 75% of the atoms are contributing magnetic moments and there are nearest neighbor magnetic atom pairs both across APBs and elsewhere [30,32]. Another possible reason is that the 1/2<100> type of APBs observed in this investigation produces second nearest neighbor like atom pairs, and the antiferromagnetic coupling of second nearest neighbor atoms is not as strong as that of first nearest neighbor atoms.

VI. Conclusions

For the present it seems that the most significant result of this research is that the ordering phase transition in the Sendust alloy occurs in a nucleation and growth process and correspondingly the microstructure in specimens quenched from the two phase region shows interfacial superlattice dislocations as well as antiphase boundaries. The density of dislocations depends on temperature, representing the lever rule for the relative amounts of each phase in the two phase region.

Thus far, this microstructural feature in the Sendust alloy has not been recognized and never been considered in discussing the dependence of magnetic properties on heat treatment conditions. Therefore, in the present research, the possible effect of the microstructure on the coercivity and the initial permeability has been qualitatively investigated in terms of the interaction of domain walls with interfacial dislocations and antiphase boundaries. However, no conclusive evidence of their interaction from in-situ studies of domain wall motion has been observed. This might be due to the fact that the interaction of domain walls with individual dislocations and APBs is not significant to be observed by Lorentz electron microscopy. Therefore, further research will be needed to determine any quantitative measurements of magnetic properties as a function of the density of those

defects.

On the other hand, grain boundaries are shown to be the most detrimental structural defects for soft magnetic applications of the Sendust alloy. Therefore, they should preferably be removed by suitable heat treatment. This result is in good agreement with the previous study on iron-silicon alloys [101], in which annealed specimens showed much higher initial permeability and lower coercivity than as-cast specimens. Although the interaction of domain walls with interfacial dislocations has not been observed, for the Sendust alloy, it might be desirable to anneal the material in the single phase region to facilitate large grains but to avoid any interfacial dislocations which would be formed at interphase interfaces in the two phase field.

The presence of inclusions and holes might also cause the coercivity to increase and the initial permeability to decrease and is likely to be undesirable. Suggestions for improving Sendust for recording heads are therefore to have clean, non-porous alloys of very large grain size, preferably single crystal.

Acknowledgments

The author would like to express his deepest appreciation to Professor Gareth Thomas for his encouragement and supervision throughout this work. Professor D. de Fontaine and D. W. Hess are also acknowledged for their time spent on his committees and reviewing this work.

The author thanks the staff of the Materials and Chemical Science Division of Lawrence Berkeley Laboratory, especially James K. Wu and John T. Holthuis, for the technical assistance. Deep appreciation is extended to Adrian Gronsky and Don J. Jurica for their helpful guidance for electron microscopy.

The author would like to thank all of his fellow graduate students who have made his stay at Berkeley quite enjoyable. The strong friendship received from Thanhtu and Lawrence are especially treasured.

This work was supported by the Director, Office of Energy Research, Office of Basic Energy Science, Division of Materials Sciences of the U. S. Department of Energy under contract No. DE-AC03-76SF00098. Financial support was obtained from Daewoo Electronics company, for which the author is grateful.

Finally, the author remains greatly obliged to his wife Haeyoung, his son Jeonghyun and Sanghyun for their indulgence during the many hours spent away from them. The author is

forever indebted to his mother, brother and sister whose constant love and encouragement made this work possible.

References

1. J. K. Howard, J. Vac. Sci. Technol. A4(1), 1 (1986)
2. B. D. Cullity, Introduction to Magnetic Materials, Addison-Wesley Publishing Co. (1972)
3. R. M. White, Science 229, 228 (1985)
4. D. E. Speliotis, IEEE Trans. Magn. MAG-20(5), 669 (1984)
5. H. Shibaya and I. Fukuda, IEEE Trans. Magn. MAG-13(3), 1005 (1977)
6. H. Senno, Y. Yamagiuchi, M. Satomi, E. Hirota and S. Hayakawa, IEEE Trans. Magn. MAG-13(5), 1475 (1977)
7. I. Yasuda, Y. Yoshisato, Y. Kawai, K. Koyama and T. Yazaki, IEEE Trans. Magn. MAG-16(5), 870 (1980)
8. I. Yasuda, Y. Yoshisato, Y. Kawai, K. Koyama and T. Yazaki, IEEE Trans. Magn. MAG-17(6), 3114 (1981)
9. N. Tsuya, K. I. Arai and K. Ohmori, IEEE Trans. Magn. MAG-15(3), 1149 (1979)
10. F. J. Jeffers, R. J. McClure, W. W. French and N. J. Griffith, IEEE Trans. Magn. MAG-18(6), 1146 (1982)
11. J. J. M. Ruigrok, IEEE Trans. Magn. MAG-20(5), 872 (1984)
12. T. Kobayashi, M. Kubota, H. Satoh, T. Kumura, K. Yamauchi and S. Takahashi, IEEE Trans. Magn. MAG-21(5), 1536

(1985)

13. C. W. M. P. Sillen, J. J. M. Ruigrok, A. Broese van Groenou and U. Enz, IEEE Trans. Magn. MAG-24(2), 1802 (1988)
14. K. Saito, T. Shimizu and H. Ishida, IEEE Trans. Magn. MAG-23(5), 2925 (1987)
15. N. Tsuya, T. Tsukagoshi, K. I. Arai, K. Ogasawara, K. Ohmori and S. Yasuda, IEEE Trans. Magn. MAG-17(6), 3111 (1981)
16. C. W. Chen, Magnetism and Metallurgy of Soft Magnetic Materials, Dover, New York (1986)
17. A. S. Zaimovski and I. P. Selissky, J. Phys. (USSR), 4(6), 563 (1941)
18. T. Wakiyama, M. Takahashi, S. Nishimaki and J. Shimoda, IEEE Trans. Magn. MAG-17(6), 3147 (1981)
19. M. Takahashi, S. Nishimaki, and T. Wakiyama, J. Magn. Magn. Mat. 66, 55 (1987)
20. I. P. Selissky, J. Phys. (USSR), 4(6), 567 (1941)
21. N. Tsuya, K. I. Arai, K. Ohmori, and M. Homma, J. Appl. Phys. 53(3), 2422 (1982)
22. T. Tanaka, K. Kaneda, and M. Homma, IEEE Trans. Magn. MAG-18(6), 1430 (1982)
23. M. Okada, Tohoku University, private communication.
24. T. Tanaka and M. Homma, IEEE Trans. Magn. MAG-21(4), 1295 (1985)
25. A. S. Zaimovsky, J. Phys. (USSR), 4(6), 569 (1941)

26. M. Takahashi, H. Arai, T. Tanaka and T. Wakiyama, IEEE Trans. Magn. MAG-22(5), 638 (1986)

27. M. Takahashi, H. Arai and T. Wakiyama, Digests of the Intermag Conference, GD-08 (1987)

28. M. Mino, T. Tanaka, and M. Homma, IEEE Trans. Magn. MAG-17(3), 1240 (1985)

29. M. Takahashi, N. Kato, T. Sato and T. Wakiyama, Digests of the Intermag Conference, EG-03 (1987)

30. J. P. Jakubovics, A. J. Lapworth and T. W. Jolly, J. Appl. Phys. 49(3), 2002 (1978)

31. K. Narita, and M. Enokizomo, IEEE Trans. Magn. MAG-15(1), 911 (1979)

32. A. P. Young and J. P. Jakubovics, J. Phys. F 5, 1866 (1975)

33. A. J. Lapworth and J. P. Jakubovics, Phil. Mag. 29, 253 (1974)

34. H. Masumoto and T. Yamamoto, J. Japan Inst. Metal 1, 127 (1937)

35. R. J. Garrod and L. M. Hogan, Acta Met. 2, 887 (1954)

36. R. H. Richman and R. G. Davis, Met. Trans. 4, 2731 (1973)

37. P. R. Swann, W. R. Duff and R. M. Fisher, Phys. Stat. Sol. 37, 577 (1970)

38. P. R. Swann, L. Granas and B. Lehtinen, Met. Sci. 9, 90 (1975)

39. H. Okamoto and P. A. Beck, Met. Trans. 2, 569 (1971)

40. P. R. Swann, W. R. Duff and R. M. Fisher, Met. Trans. 3,

409 (1972)

41. P. R. Swann and R. M. Fisher, Appl. Phys. Letters, 9, 279 (1966)
42. P. R. Swann, W. R. Duff and R. M. Fisher, Trans. TMS-AIME 245, 851 (1969)
43. S. M. Allen and J. W. Cahn, Acta Met. 24, 425 (1976)
44. R. B. Griffiths, J. Chem. Phys. 60, 195 (1974)
45. G. Inden and W. Pitsch, Z. Metallkunde 62, 627 (1971)
46. P. S. Rudman, Acta Met. 8, 321 (1960)
47. G. Inden and W. Pitsch, Z. Metallkunde 63, 253 (1972)
48. M. J. Marcinkowski, in EM and Strength of Crystals (edited by G.Thomas), 360 (1963)
49. M. J. Marcinkowski and N. Brown, J. Appl. Phys. 33(2), 537 (1962)
50. M. J. Marcinkowski and N. Brown, Acta Met. 9, 764 (1961)
51. R. C. Crawford, I. L. F. Ray and D. J. H. Cockayne, Phil. Mag. 27, 1 (1973)
52. I. L. F. Ray, R. C. Crawford and D. J. H. Cockayne, Phil. Mag. 21, 1027 (1970)
53. D. J. H. Cockayne, I. L. F. Ray and M. J. Whelan, Phil. Mag. 20, 1265 (1969)
54. M. J. Marcinkowski and R. M. Fisher, J. Appl. Phys. 31, 1687 (1960)
55. R. M. Fisher and M. J. Marcinkowski, Phil. Mag. 6, 1385 (1961)
56. M. J. Whelan and P. B. Hirsch, Phil. Mag. 2, 1121 (1957)

57. M. J. Whelan and P. B. Hirsch, Phil. Mag. 2, 1303 (1957)

58. L. E. Tanner and H. J. Leamy, Proc. of the International Symposium on Order-Disorder Transformations in Alloys, edited by H. Warlimont, New York, 180 (1974)

59. D. de Fontaine, Solid State Physics, edited by H. Ehrenreich, F. Seitz and D. Turnbull, vol. 34, Academic Press, New York (1979)

60. L. D. Landau and E. M. Lifshitz, Statistical Physics, Addison-Wesley, Reading, MA (1958)

61. M. Sluiter, P. Turchi, Fu Zezhong and D. de Fontaine, Physica 148A, 61 (1988)

62. Y. J. Chang, Acta Met. 30, 1185 (1982)

63. M. Takahashi and T. Wakiyama, MRS proceedings to be published (1988)

64. M. G. Mendiratta and S. K. Ehlers, Met. Trans. 14A, 2435 (1983)

65. H. Warlimont and G. Thomas, Metal Sci. J. 4, 47 (1970)

66. M. J. Blackburn, Trans. AIME 239, 1200 (1967)

67. S. G. Cupschalk and N. Brown, Acta Met. 16, 657 (1968)

68. H. J. Leamy, P. Schwellinger and H. Warlimont, Acta Met. 18, 31 (1970)

69. J. D. Livingston, Prog. Mater. Sci. 7, 243 (1981)

70. A. L. Stuijtx, Ceramic Microstructure, in Proc. 6th Int. Mat. Symp., R. M. Fulrath and J. A. Pask, Eds. Boulder, Co. (1977)

71. P. J. Grundy and R. S. Tebble, Advances in Physics 17,

153 (1968)

72. C. R. Barrett, W.D. Nix and A.S. Tetelman, The Principles of Engineering Materials, Prentice-Hall, Inc. (1973)
73. C. Kittel and J. K. Galt, Solid State Physics, Ed. Seitz and Turnbull, Academic Press, New York (1956)
74. R. M. Bozorth, Ferromagnetism, Van Nostrand, New York (1951)
75. D. J. Craik and R. S. Tebble, Rep. Progr. Phys. 24, 116 (1961)
76. E. H. Kennard, Phys. Rev. 55, 312 (1939)
77. M. E. Hale, H. W. Fuller and H. Rubinstein, J. Appl. Phys. 30, 789 (1959)
78. L. Marton, Phys. Rev. 73, 1475 (1948)
79. L. Mayer, J. Appl. Phys. 28, 975 (1957)
80. G. Thomas and M. J. Goringe, Transmission Electron Microscopy of Materials, John Willey & Sons, New York (1979)
81. J. W. Edington, Practical Electron Microscopy in Materials Science, Monograph Three, McMillan Press Ltd., London (1975)
82. P. Hirsch, A. Howie, R. B. Nicholson, D. W. Pashley and M. J. Whelan, Electron Microscopy of Thin Crystals, 2nd edition, Robert E. Krieger Publishing Co., New York (1977)
83. J. T. Michalak and R. C. Glenn, J. Appl. Phys. 32(7), 1261 (1961)

84. Philips Scientific and Analytic Equipment Service Manual PW 6002

85. H. W.Fuller and M. E. Hale, J. Appl. Phys. 31 (2), 238 (1960)

86. J. Silcox, Phil. Mag. 8, 7 (1963)

87. S. R. Herd, K. Y. Ahn and S. M. Kane, IEEE Trans. Magn. MAG-15(6), 1824 (1979)

88. C. Kittel, Phys. Rev. 70, 965 (1946)

89. S. Chikazumi, Physics of Magnetism, Wiley, London (1964)

90. M. Prutton, Phil. Mag. 5, 625 (1960)

91. J. B. Goodenough, Phys. Rev. 95, 917 (1954)

92. I. N. Lin, R. K. Mishra and G. Thomas, IEEE Trans. Magn. MAG-20(1), 134 (1984)

93. L. F. Bates and R. Carey, Proc. Phys. Soc. 75, 880 (1960)

94. R. S. Tebble, Proc. Phys. Soc. B68, 1017 (1955)

95. H. J. Williams and W. Shockley, Phys. Rev. 75, 178 (1949)

96. A. Seeger, H. Kronmuller, H. Rieger and H. Trauble, J. Appl. Phys. 35, 740 (1964)

97. D. E. Scherpereel, L. L. Kazmerski and C. W. Allen, Met. Trans. 1, 517 (1970)

98. A. J. J. Koch, P. Hokkeling, M. G. Steeg and K. J. de Vos, J. Appl. Phys., 31, 75S (1960)

99. H. Zijlstra and H. B. Haanstra, J. Appl. Phys. 37 (7), 2853 (1966)

100. A. J. Lapworth, J. P. Jakubovics and G. S. Baker, J. Phys. Paris 32, C1-259-60 (1971)

101.T. Miyazaki, M. Takahashi, K. Takakura and T. Ito, J. Magn. Magn. Mat. 24, 279 (1981)

Tables

Table 1. Phase shifts for antiphase vectors in DO_3 phase

h k l	type of reflection	phase shift (α) 1/4 <111>	1/2<100>
111	S	$\pm\pi/2$	$\pm\pi$
200	S	$\pm\pi$	0
220	F	0	0
311	S	$\pm\pi/2$	$\pm\pi$
222	S	$\pm\pi$	0
400	F	0	0

F : Fundamental reflection

S : Superlattice reflection

Table 2. Predominant contrast expected from the phases in the hkl dark field images [38]

Reflection	Phase: Disordered bcc	B2	DO_3
h + k + l = 4N	Light	Light	Light
h + k + l = 2N	Dark	Light	Light
h + k + l = N	Dark	Dark	Light

Note : The indices for all phases are referred to the axes of the unit cell shown in figure 3b.

N = an odd integer. The integers h,k and l are either all even or all odd.

Table 3. Nearest- and next-nearest-neighbor arrangements for ordered $Fe_3(Si,Al)$ alloy, based on sublattice sites shown in figure 3b.

	B2		DO_3	
	N-N	N-N-N	N-N	N-N-N
Fe_{III}	8 Fe	-	8 Fe	6 Si(Al)
Fe_{II}	4 Fe	-	4 Fe	6 Fe
	4 Si(Al)		4 Si(Al)	
$Si(Al)_I$	8 Fe	-	8 Fe	6 Fe

Figure Captions

Figure 1. Principle of writing and reading transitions using an inductive head and a longitudinal moving medium [1].

Figure 2. Phase diagrams of (a) iron-aluminum [40] and (b) iron-silicon [38] alloys.

Figure 3. Unit cells of (a) the B2 and (b) the DO_3 superlattice [48].

Figure 4. Heat treatment processes: (a) isothermal (b) step quenching.

Figure 5. Dark-field micrographs using the 111 superlattice reflection in (a) an as-cast specimen, (b) a specimen held for 1 hr at 1032°C and then quenched, and (c) a tableau of selected area diffraction patterns (SADPs) from both specimens. These SADPs indicate that both specimens consist of single phase DO_3.

Figure 6. Analysis of the type of the antiphase boundary (APB) in the DO_3 ordered phase of an $Fe_3Si_{0.6}Al_{0.4}$ Sendust alloy. APBs are clearly shown in the 111 superlattice reflection in dark bands contrast (a) but the contrast vanishes in the 200 superlattice reflection (b), showing the type of APBs is 1/2<100>.

Figure 7. Dark-field micrographs in a specimen held for 1hr

at 1025°C and quenched. The 111 superlattice reflection revealed APB contrast (a), while the 222 superlattice reflection revealed only dislocations at which APBs terminated (b).

Figure 8. Microstructures in a specimen held for 1/2 hr at 1,100°C, furnace-cooled to 1,030°C, held for 1 hr, and then quenched into iced brine, showing the antiphase domain structure of the DO_3 phase without dislocations.

Figure 9. Same heat treatment as in figure 8 but with a quenching temperature of 1026°C, showing dislocations formed at a boundary.

Figure 10. Same heat treatment as in figure 9, showing APBs (a) and dislocations (b) delineating a morphology like second phase particle.

Figure 11. Same heat treatment as in figure 8 but with a quenching temperature of 1024°C, showing the growth of DO_3 domains which originated at APBs of the former B2 phase.

Figure 12. Same heat treatment as in figure 11 showing the former B2 phase transformed to the DO_3 phase during quenching. APBs terminated at the interface.

Figure 13. Same heat treatment as in figure 11 showing interfacial superlattice dislocations bound with APBs in the DO_3 ordered phase. The 111

superlattice reflection revealed the APB contrast(a), whereas the fundamental reflection of 220 type revealed only interfacial dislocations (b). At the quenching temperature the atomic displacements in the direction of 1/2<100> do not produce APBs because they are not the antiphase vector in the B2 phase. Therefore, APBs are indicated by broken lines in the B2 phase (c).

Figure 14. Contrast analysis to determine the type of the Burgers vector of interfacial dislocations. Dislocations are invisible in 400 reflections (a and b) but visible in 022 (c) and 202 (d) reflections, showing that the type of the Burgers vector is 1/2<001>.

Figure 15. Same heat treatment as in figure 8 but with a quenching temperatue of (a) 960°C and (b) 900°C, showing a decrease in domain size of the former B2 phase with decreasing quenching temperature.

Figure 16. Microstructures in specimens held for 1 hr at (a) 1100°C, (b) 1045°C and (c) 1,040°C, and then quenched into iced brine. The 220 type reflections show interfacial dislocations in (a) and (b).

Figure 17. Domain structure of a single crystal slab of iron (a) in the unmagnetized state; (b) after reversible movements of domain walls; (c) after irreversible movements of domain walls; (d) after

Figure 24. Same as in figure 19 showing closure domains formed at a crack and showing cross-tie walls. Assumed magnetization directions are indicated by arrows in a schematic diagram (b).

Figure 25. Sections parallel to film surface of (a) a hypothetical Neel wall with sections of opposite polarity, and (b) a cross-tie wall [2].

Figure 26. Effect of APBs on the magnetic domain structure in an $Fe_3Si_{0.6}Al_{0.4}$ Sendust alloy. Overfocused (a) and underfocused (b) Lorentz images taken with objective lens off show that a domain wall passes straight across APBs.

Figure 27. Effect of interfacial dislocations on the magnetic domain structure. Overfocused (a) and underfocused (b) Lorentz images taken with objective lens off show that a domain wall passes straight across the interfacial dislocations marked by arrows.

Figure 28. Interaction of domain walls with interfacial dislocations and APBs. Specimen tilting caused a domain wall to move in the direction of the arrow and then successively through interfacial dislocations and APBs without any deflection. Overfocused and underfocused Lorentz images in (a), (b), (c) and (d) taken with objective lens off represent each stage of magnetization.

Figure 29. Effect of a grain boundary on the magnetic domain

structure. With the objective lens off a closure domain C formed at a grain boundary and the domain wall A was deflected at the grain boundary.

Figure 30. Same as in figure 29 but with the objective lens on. A segment of domain wall B in figure 29 was pinned at the grain boundary, while domain wall A moved in the direction of the arrow.

Figure 31. Specimen tilting with the objective lens on caused domain walls in figure 30 to move in the direction of the arrow. A larger segment of domain wall B was pinned at the grain boundary and a new closure domain formed at C'. Reference mark D indicates that all micrographs are from the same area.

Figure 32. Overfocused (a) and underfocused (b) Lorentz images taken with objective lens off showing reverse domains formed at a hole.

Figure 33. Interaction of domain walls with a hole. Overfocused (OF) and underfocused (UF) Lorentz images with schmatic diagrams in each stage of magnetization show that reverse domains formed at a hole caused the domain wall to be bulged in the direction opposite to the wall motion. Specimen tilting with the objective lens off caused the domain wall to move in the direction of the arrow.

Figure 34. Overfocused (a) and underfocused (b) Lorentz images with the objective lens off showing

reverse domains formed at an inclusion.

Figure 35. Schematic diagram illustrating the dependence of magnetic energy of an inclusion on the position of a boundary wall [73].

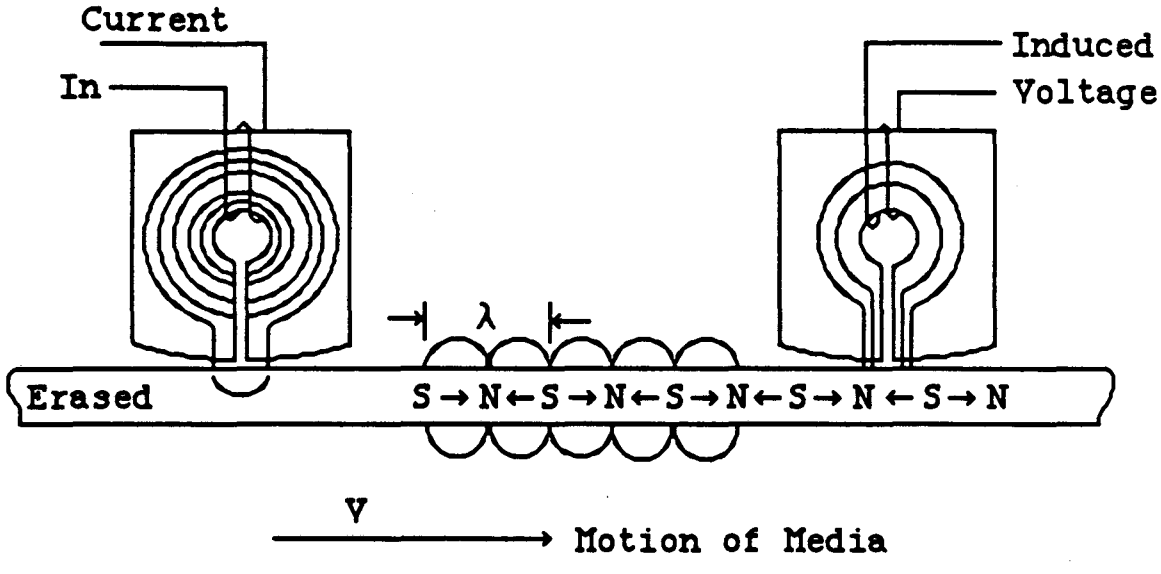
Current
In
Induced
Voltage
λ
Erased
S → N ← S → N ← S → N ← S → N ← S → N
V
Motion of Media
Writing
Reading
XBL 8811-3791

Figure 1

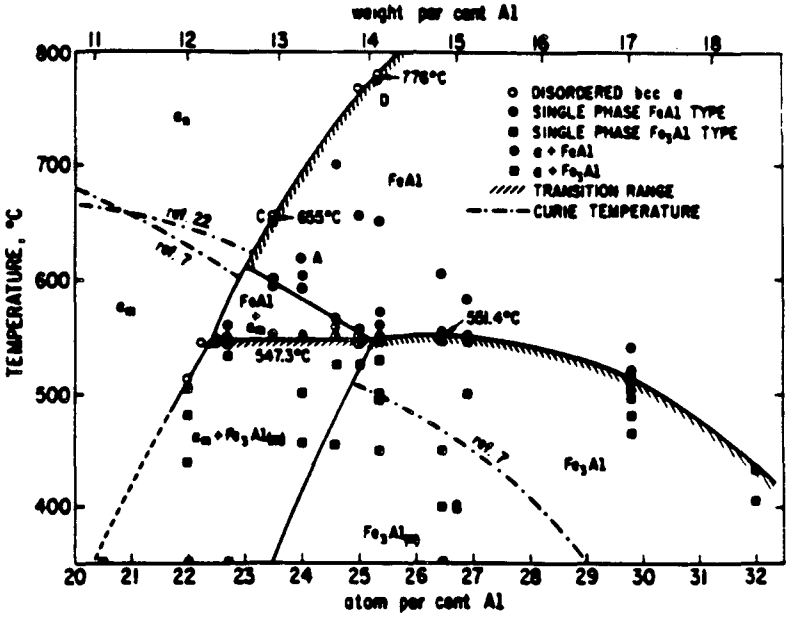

(a)

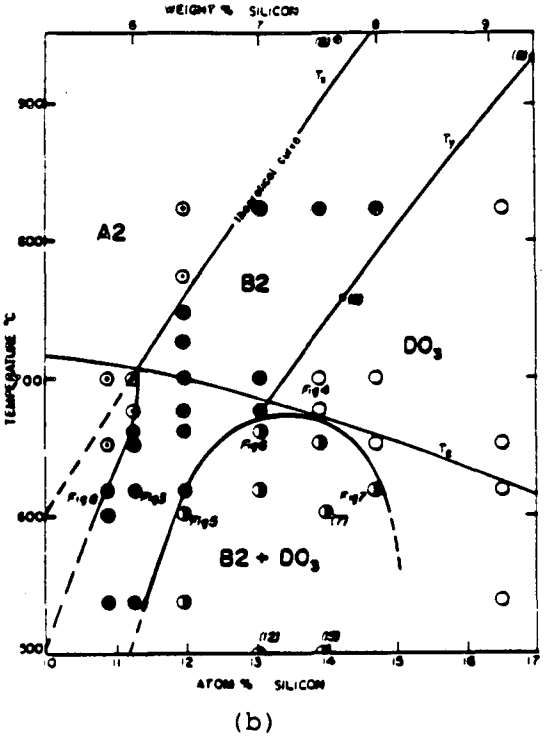

(b)

XBL 8811-3790

Figure 2

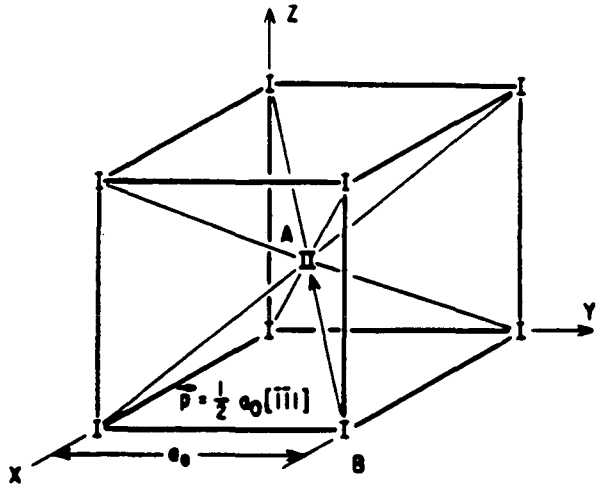

(a)

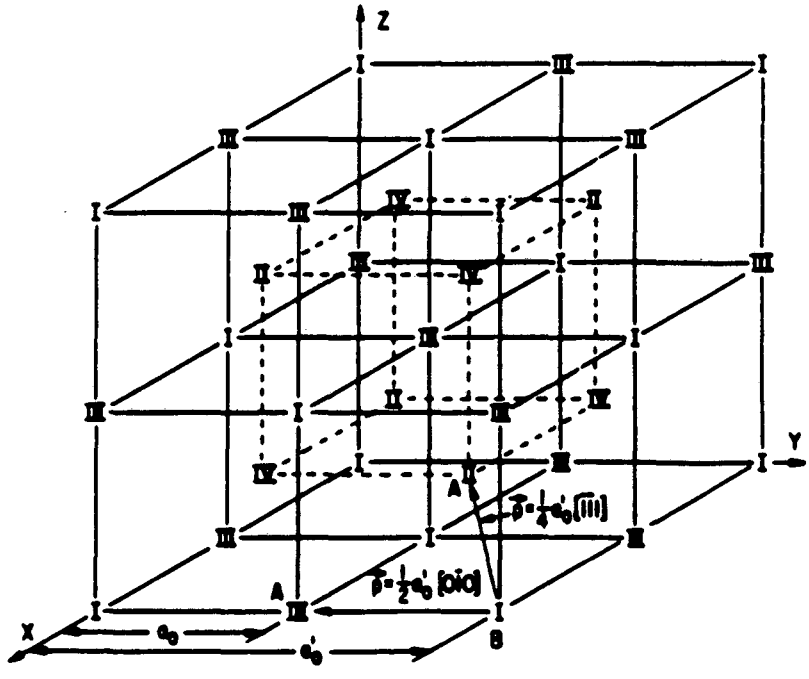

(b)

XBL 8811-3792

Figure 3

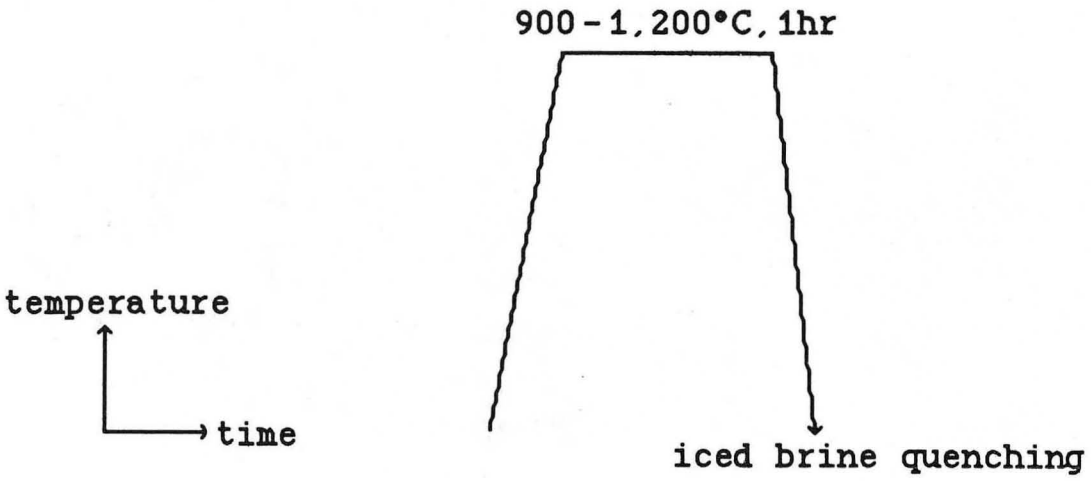

(a)

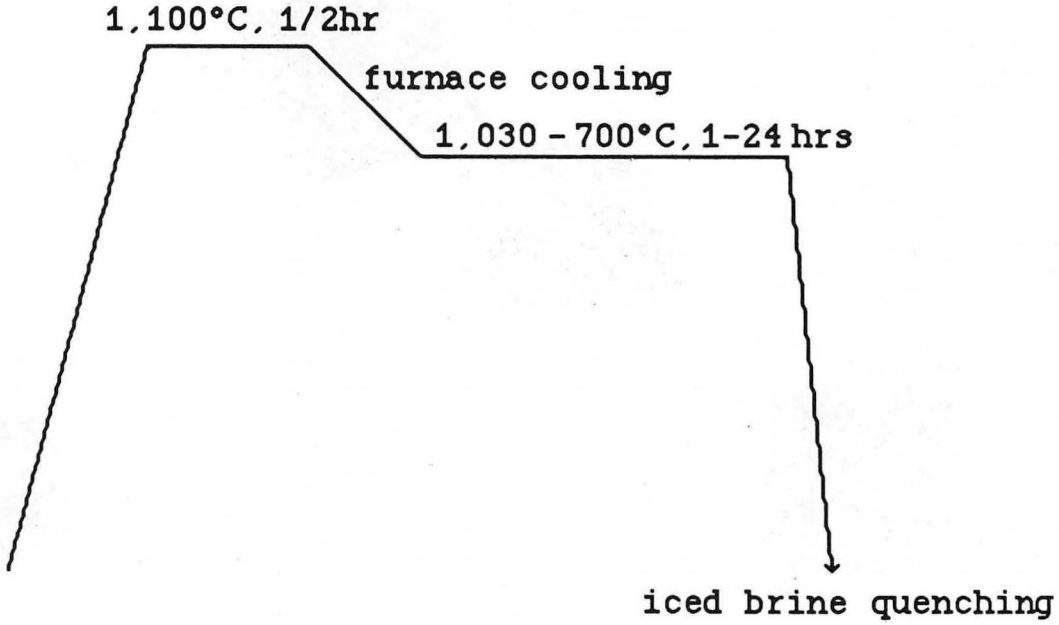

(b)

XBL 8811-3793

Figure 4

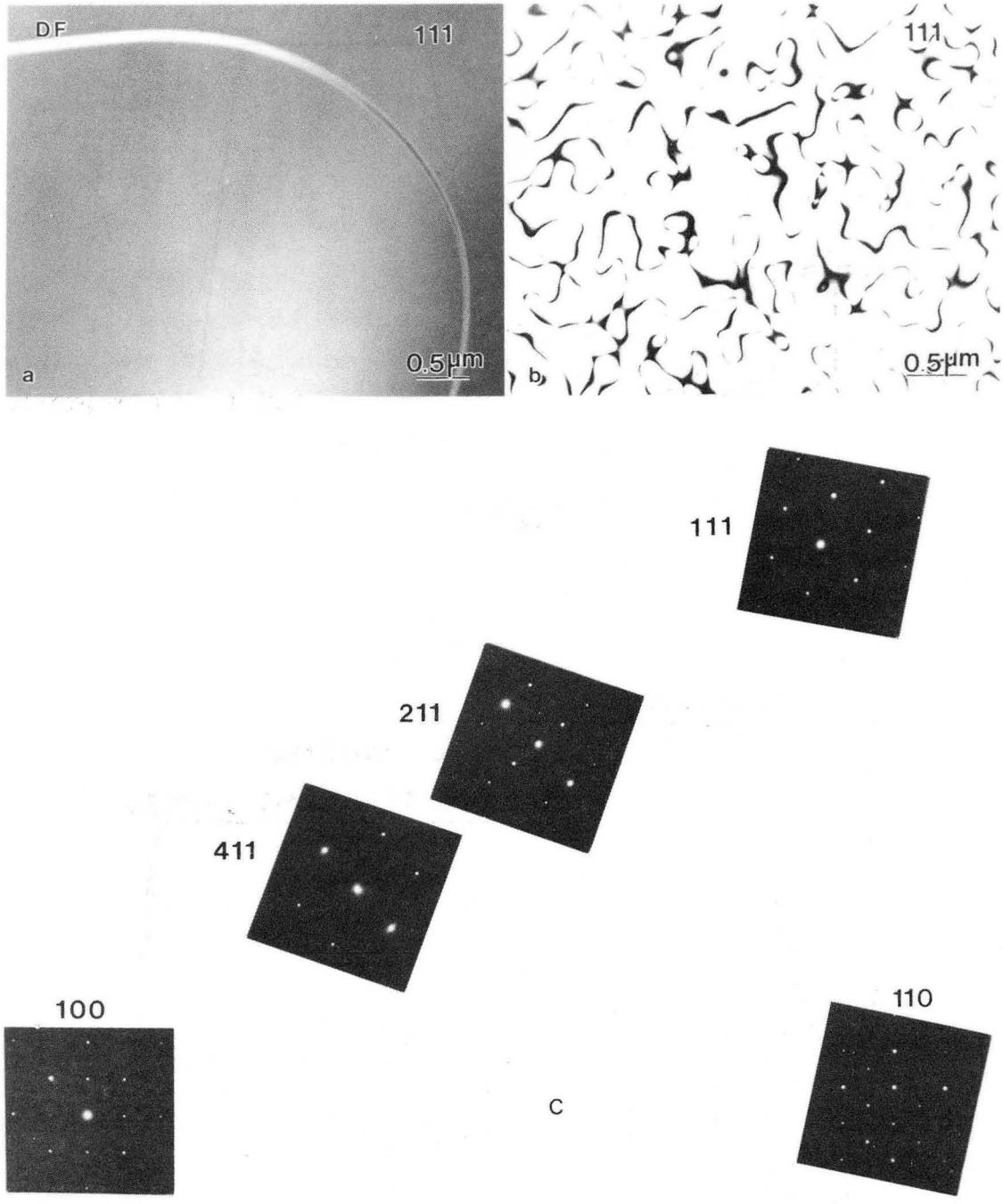

Figure 5

XBB 881-43-B

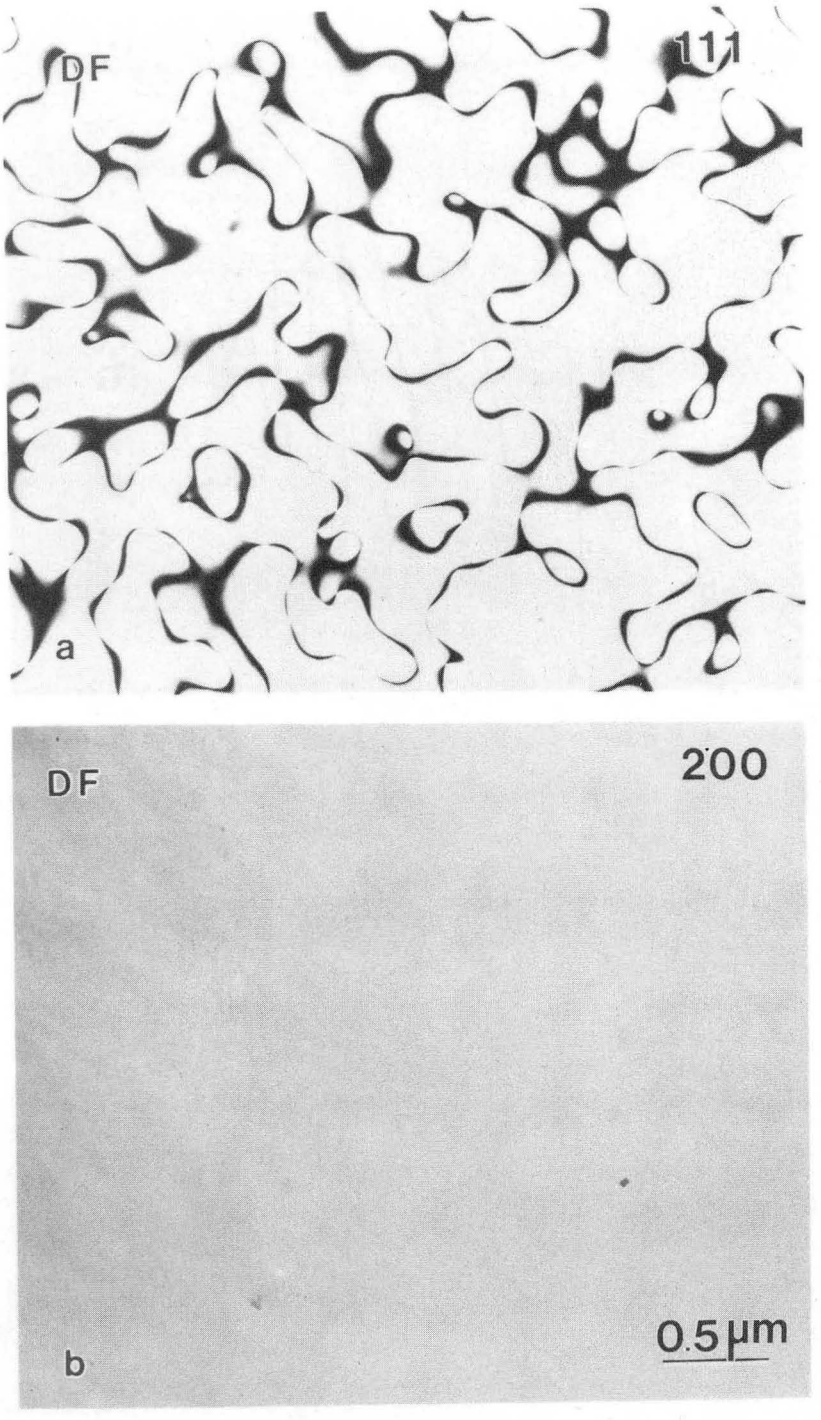

XBB 885-5242-A

Figure 6

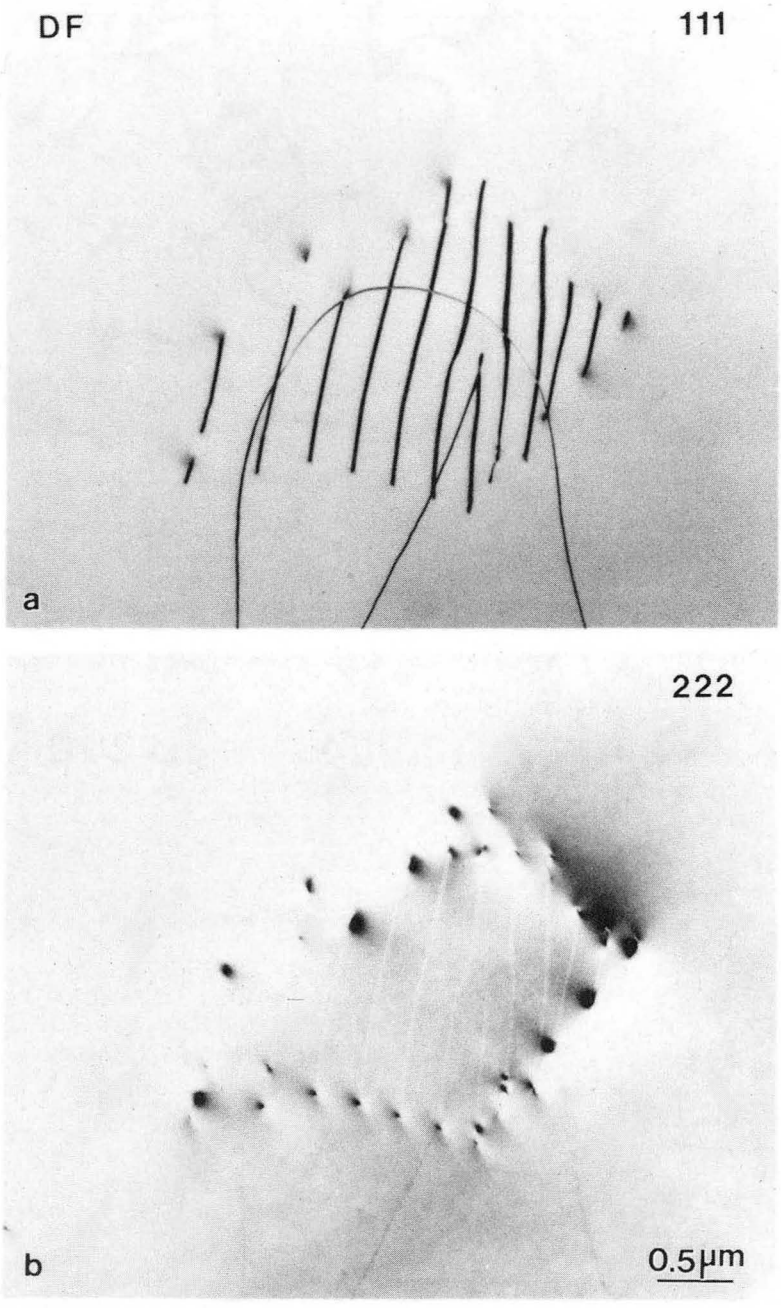

XBB 888-7361-A

Figure 7

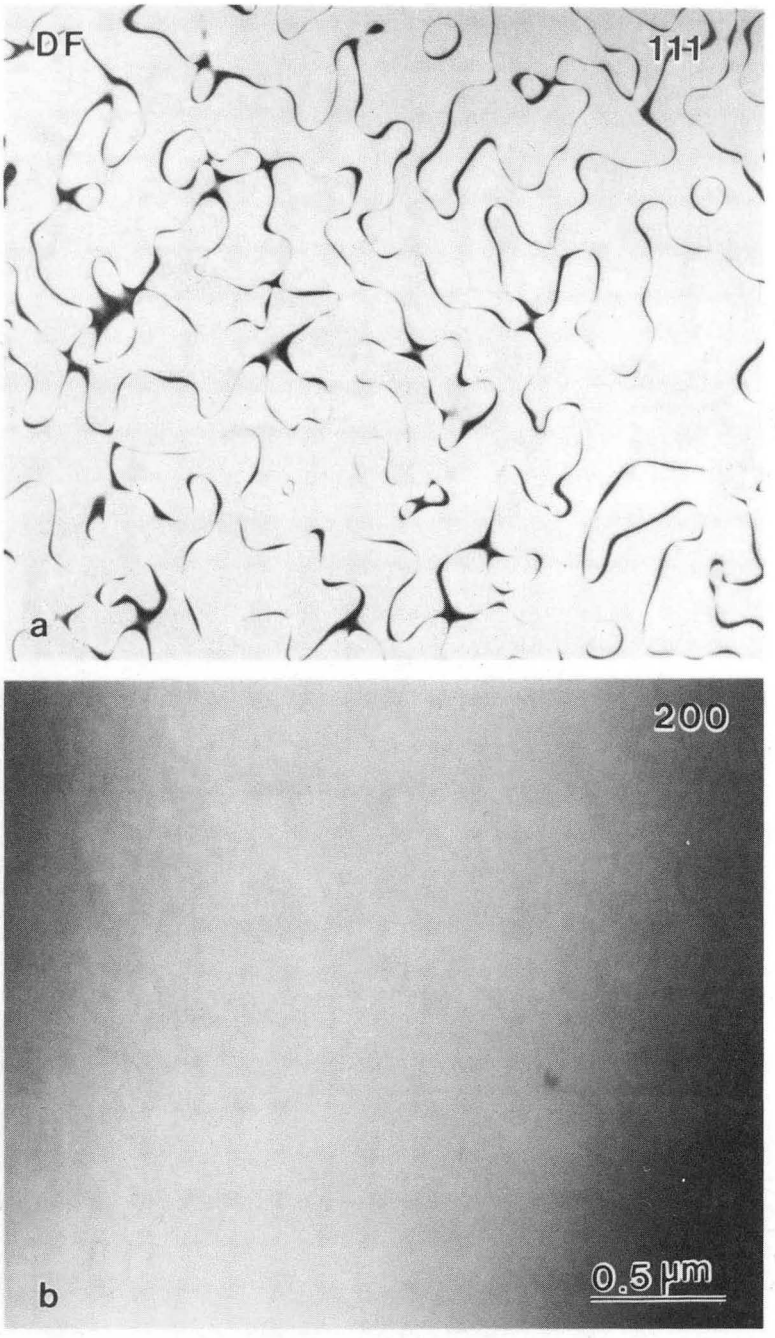

XBB 880-10649

Figure 8

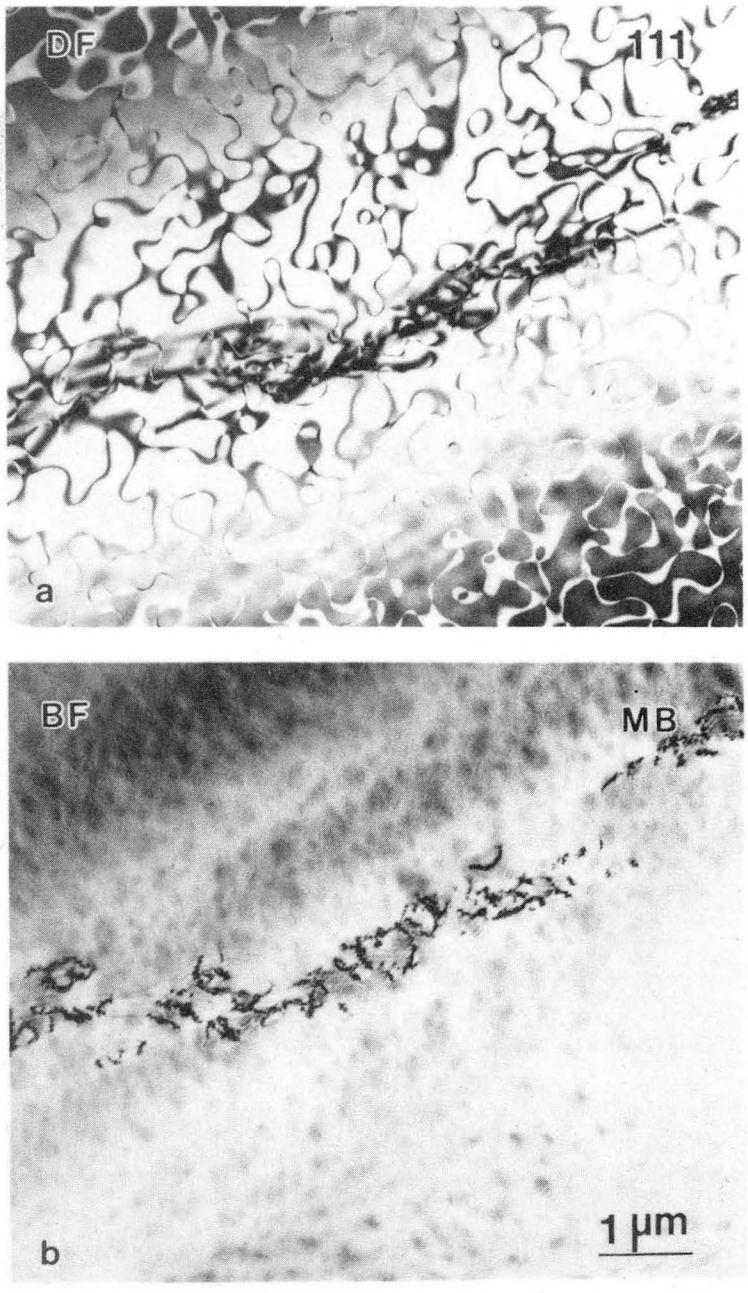

XBB 881-45-A

Figure 9

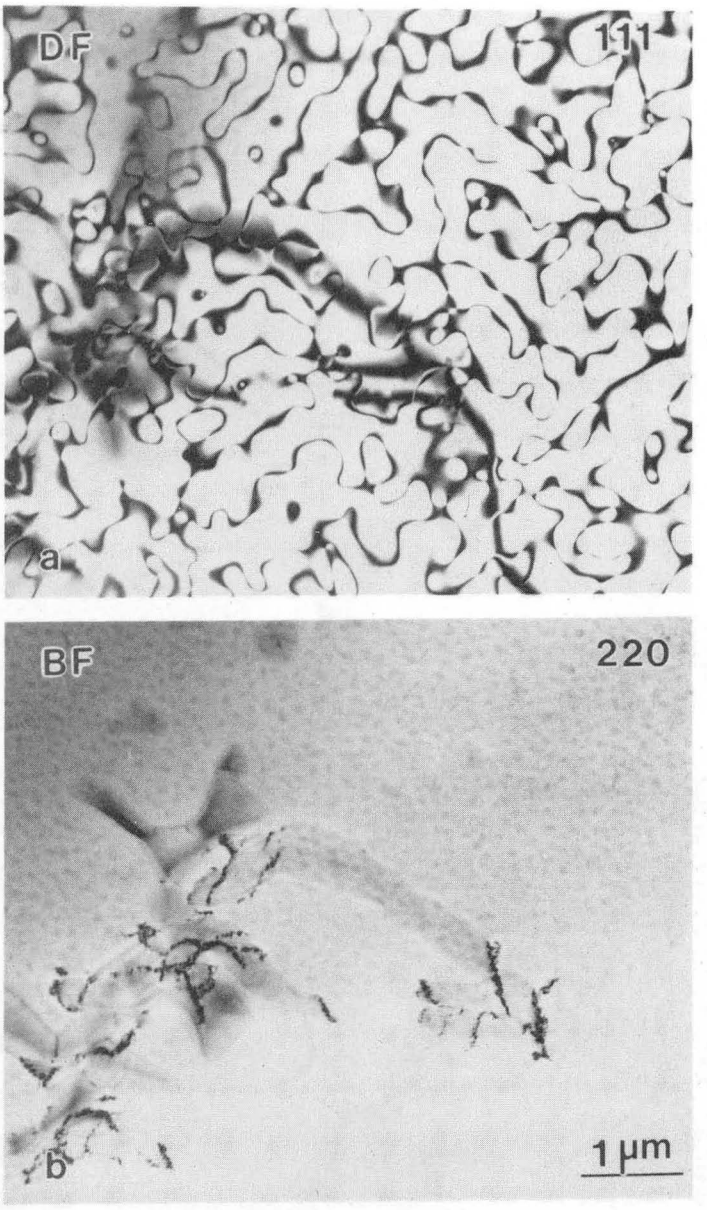

XBB 881-45-B

Figure 10

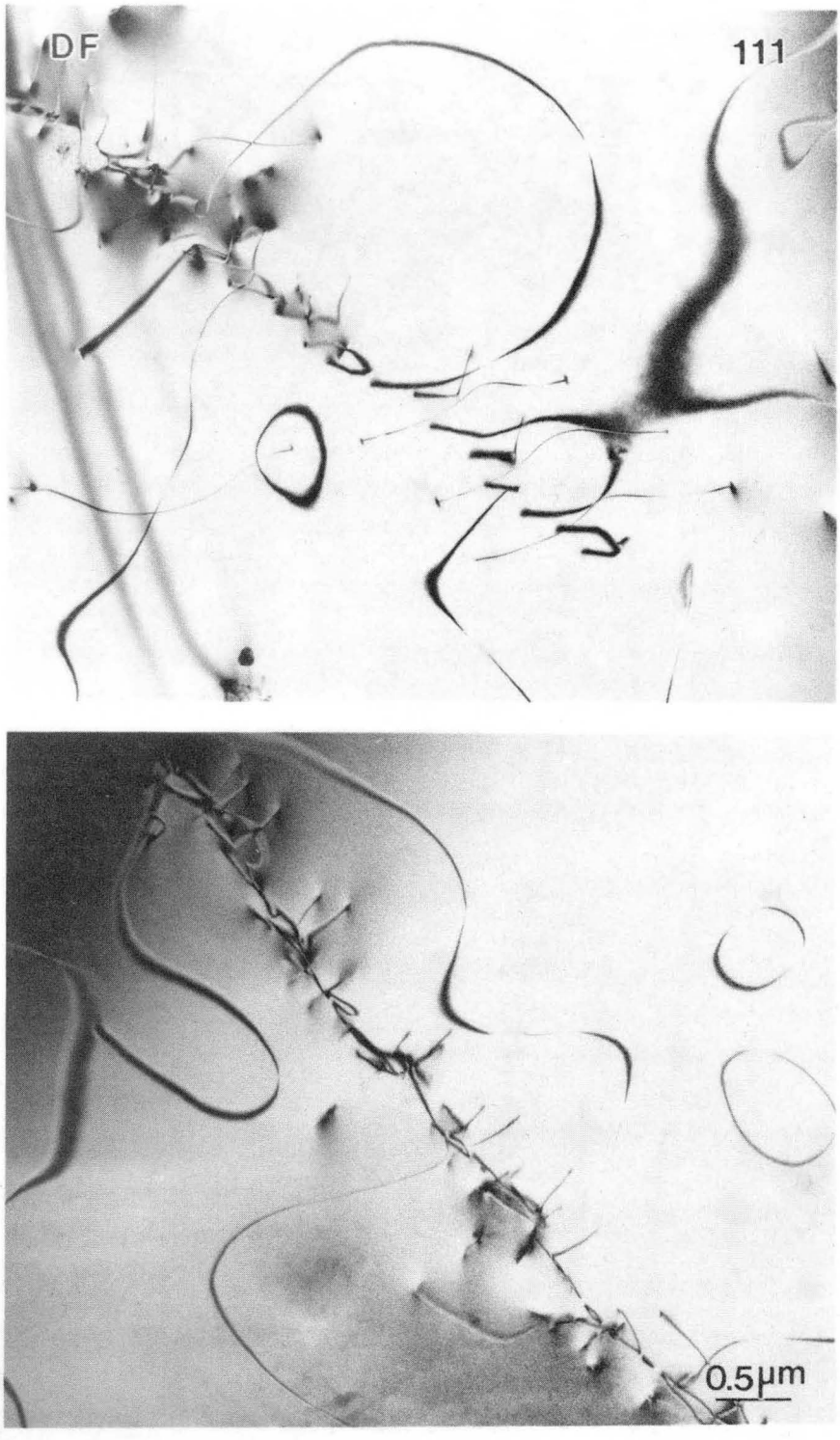

XBB881-47-A

Figure 11

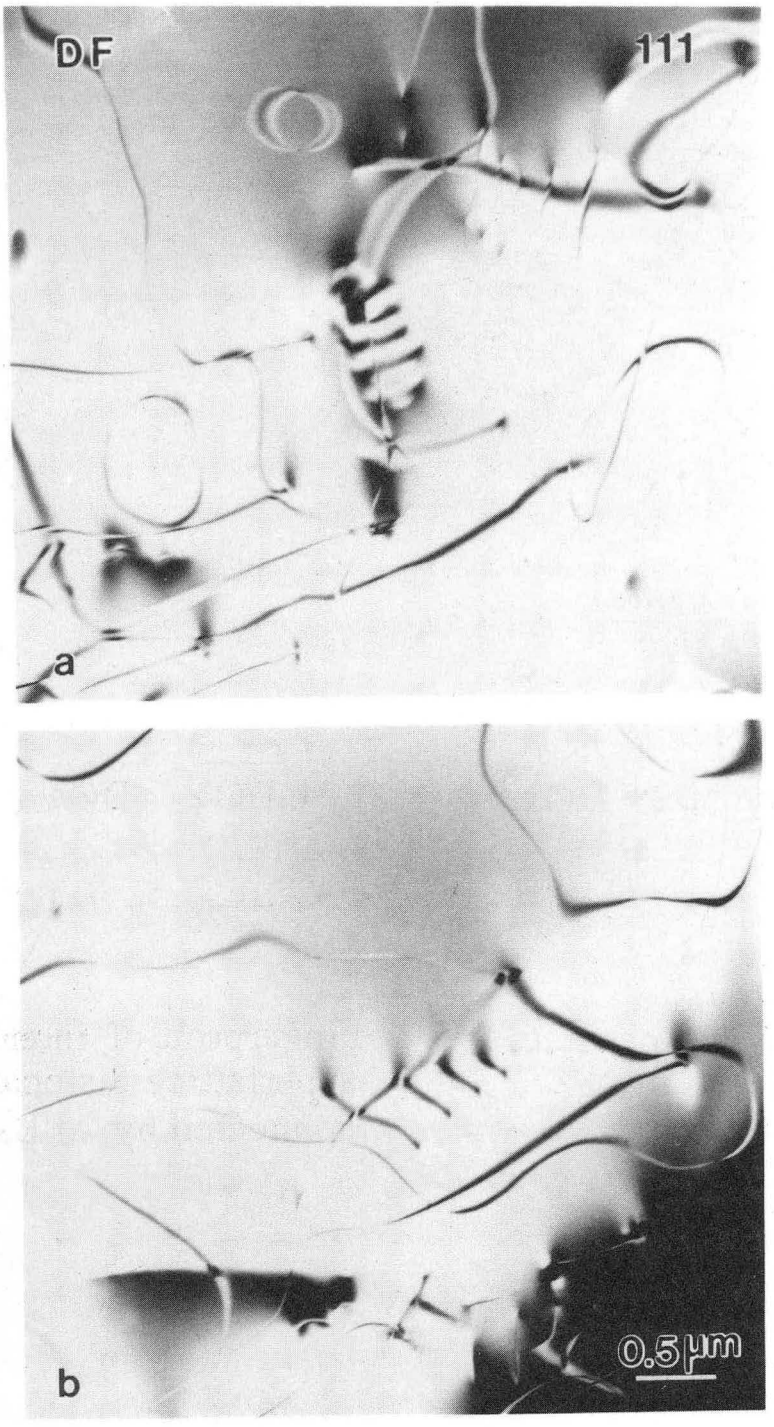

XBB881-46-A

Figure 12

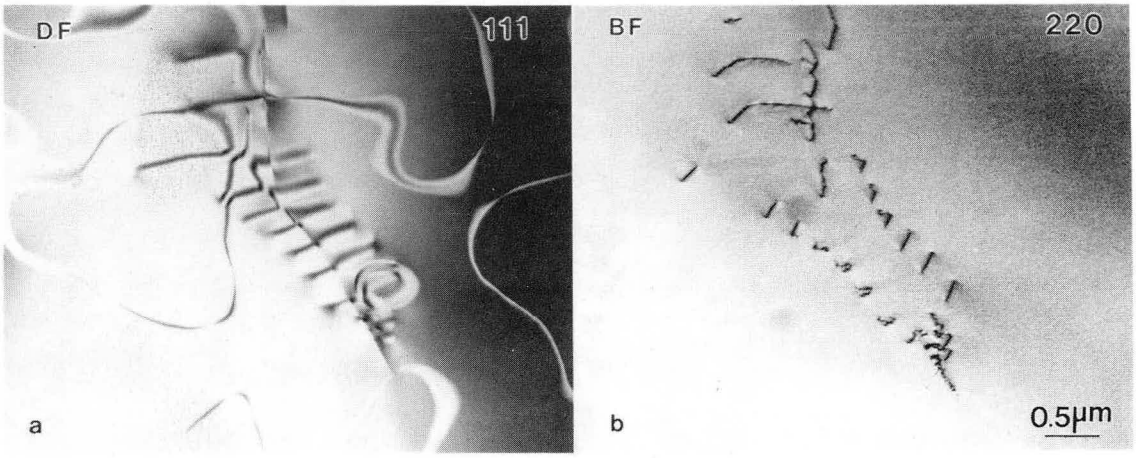

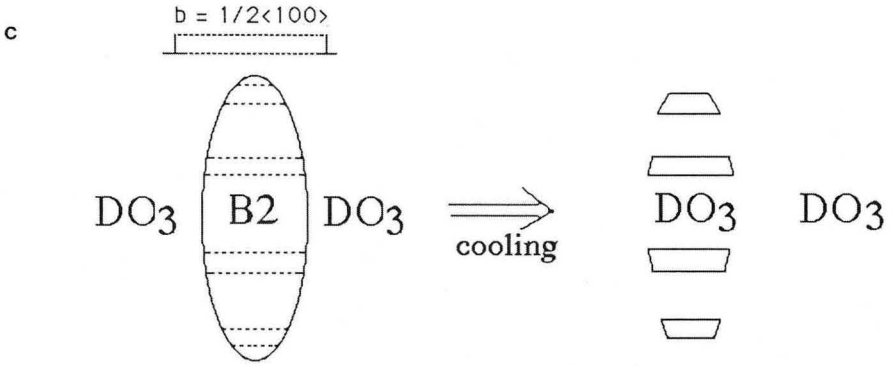

Original particle
B2 -> DO_3

Fingerprint of interfacial superlattice dislocations connected by APBs

Figure 13

XBB882-816A

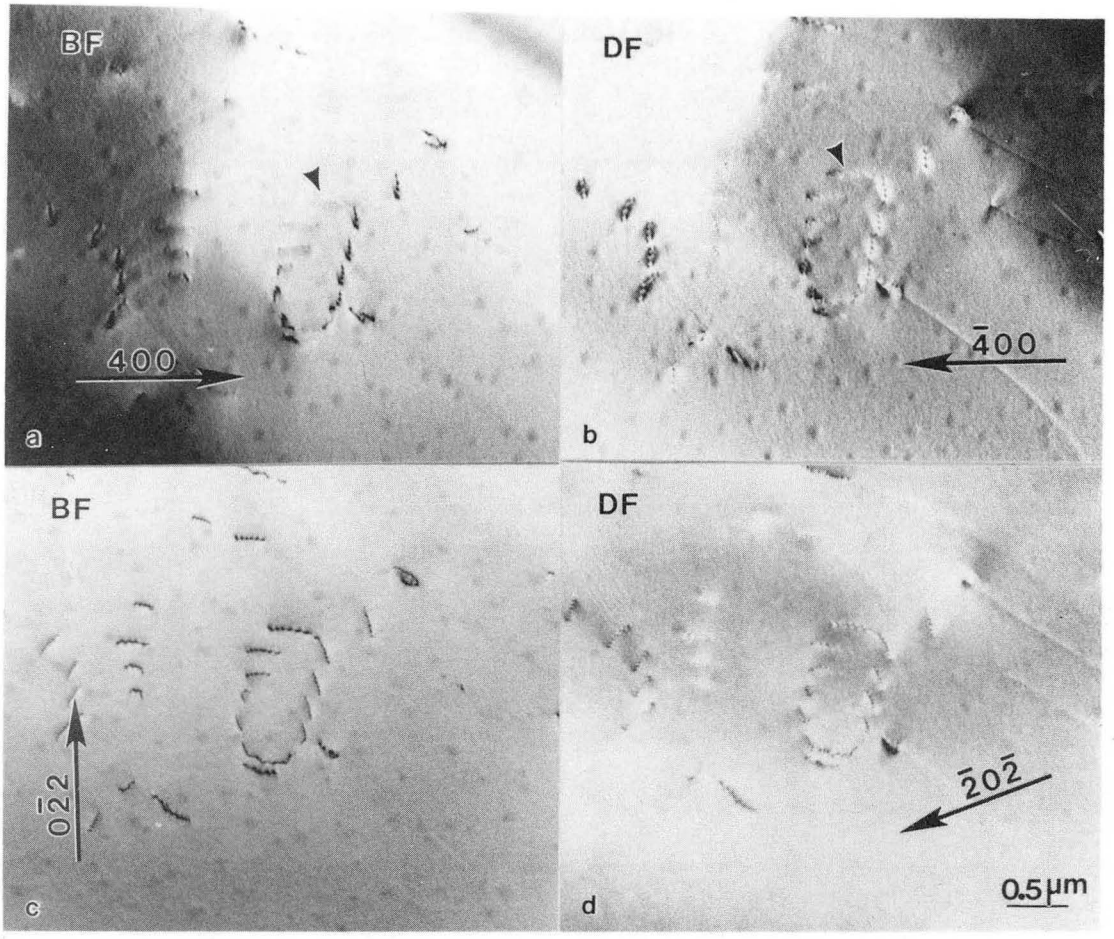

XBB881-463-A

Figure 14

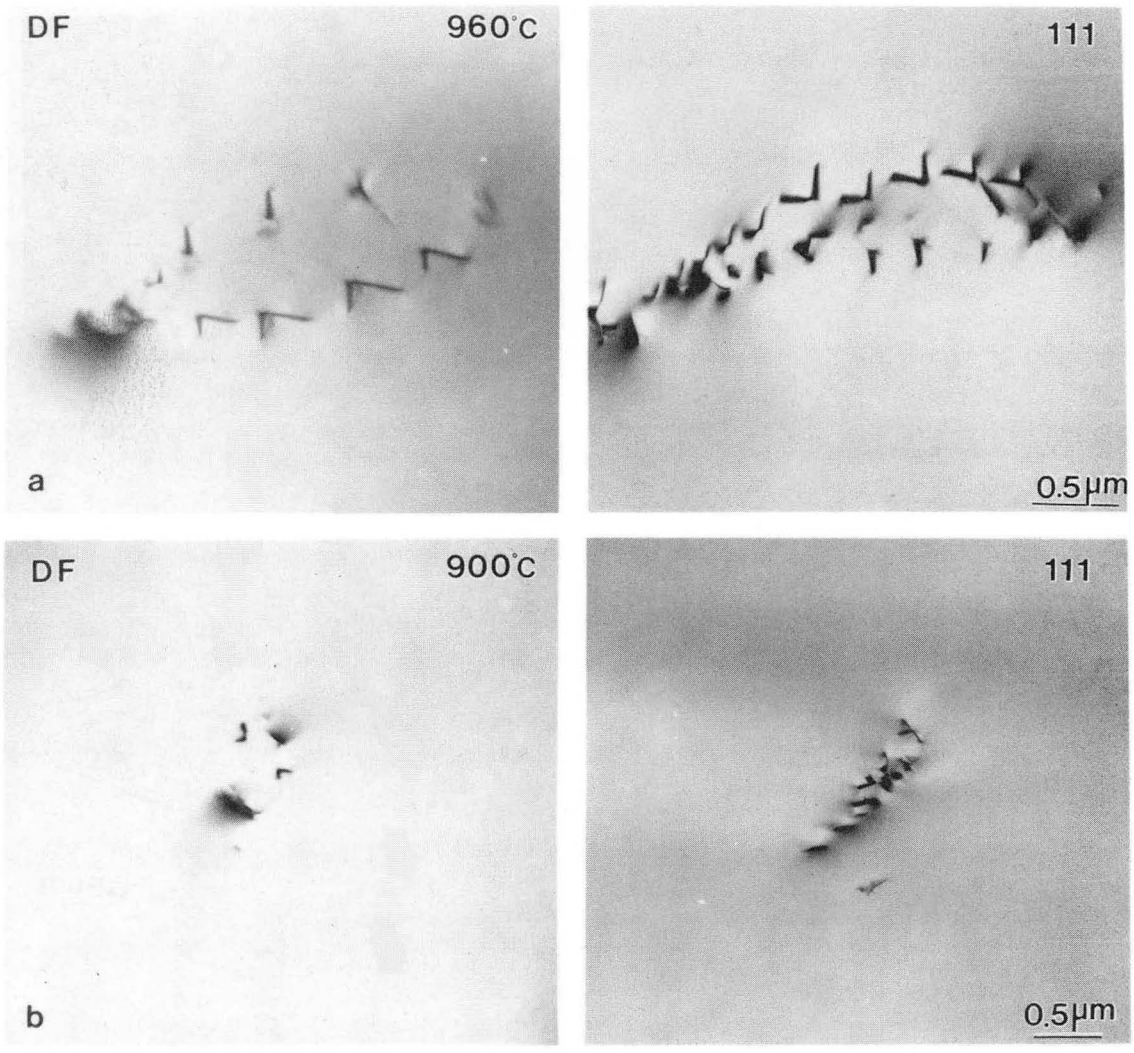

XBB881-44-A

Figure 15

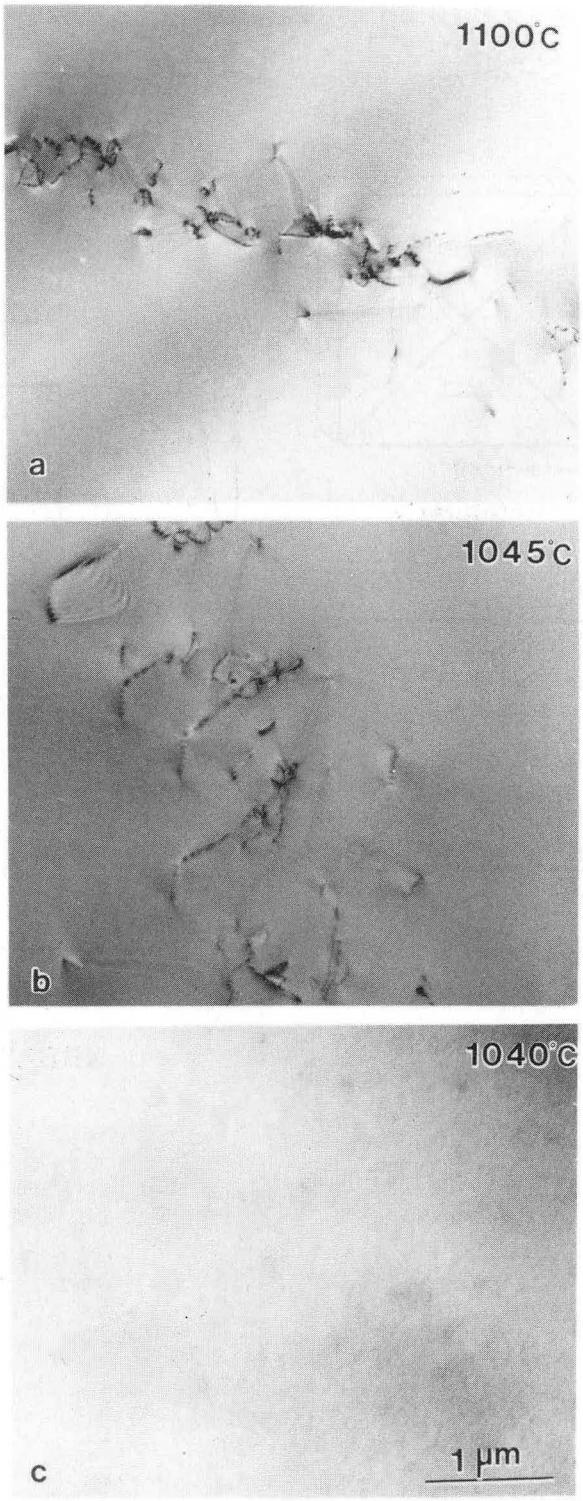

XBB881-48-A

Figure 16

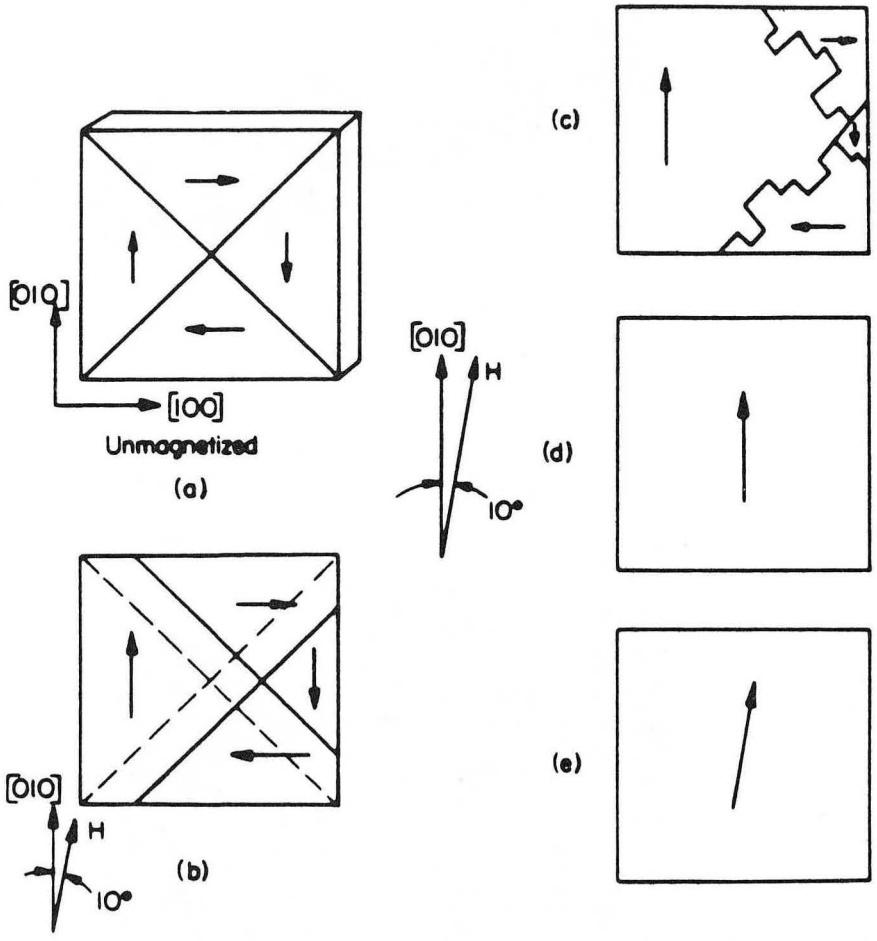

XBL 8811-3794

Figure 17

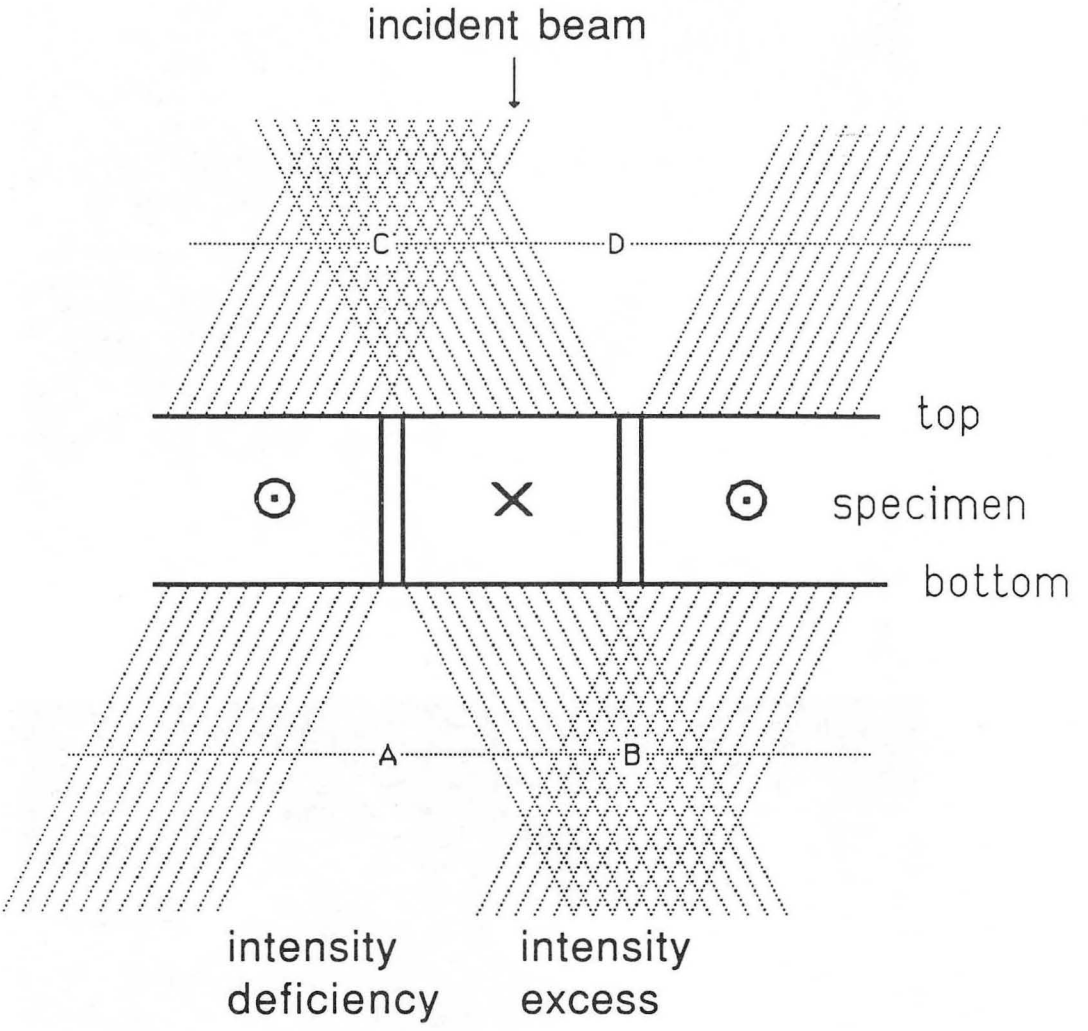

XBL 8811-3795

Figure 18

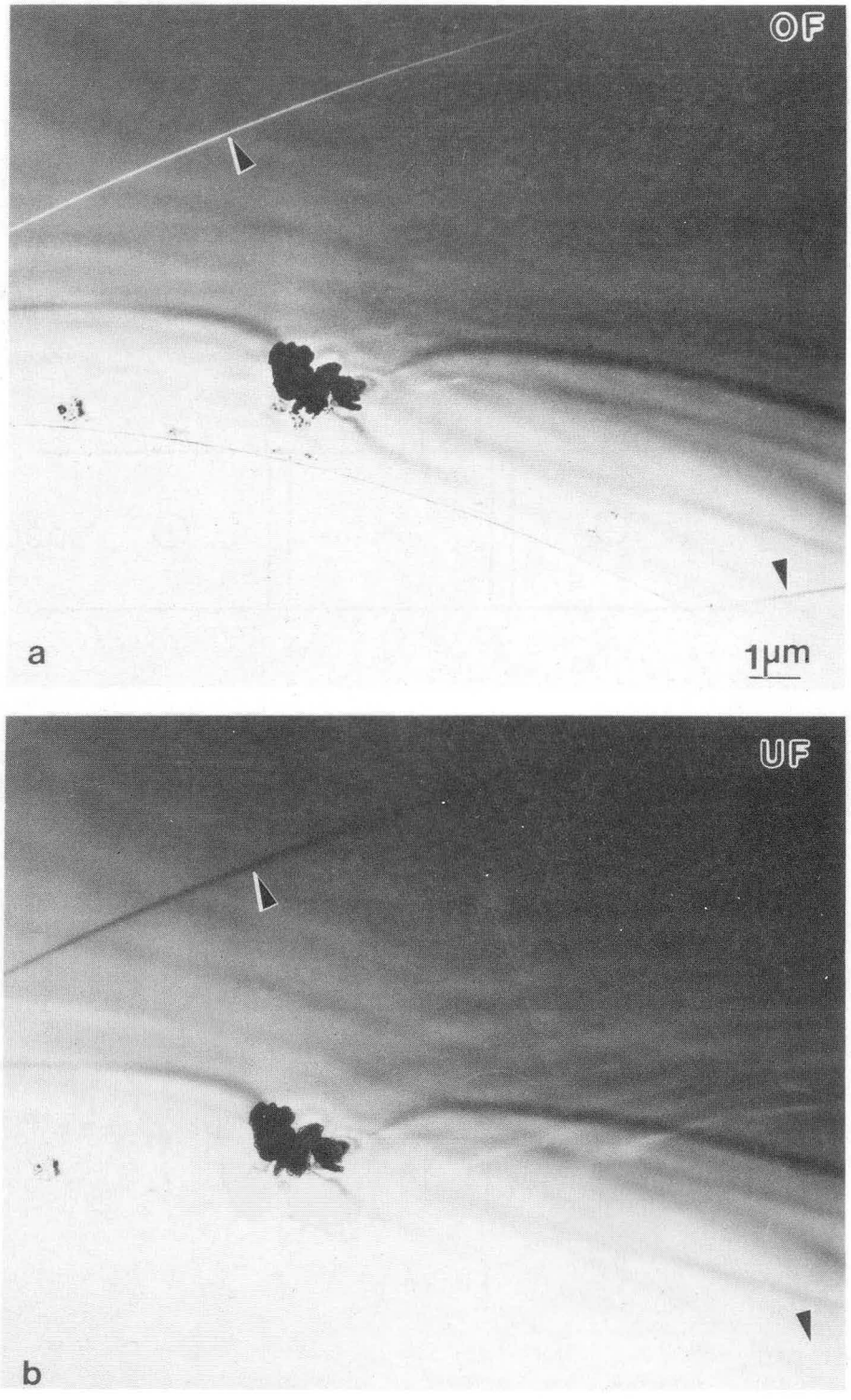

XBB889-8703-A

Figure 19

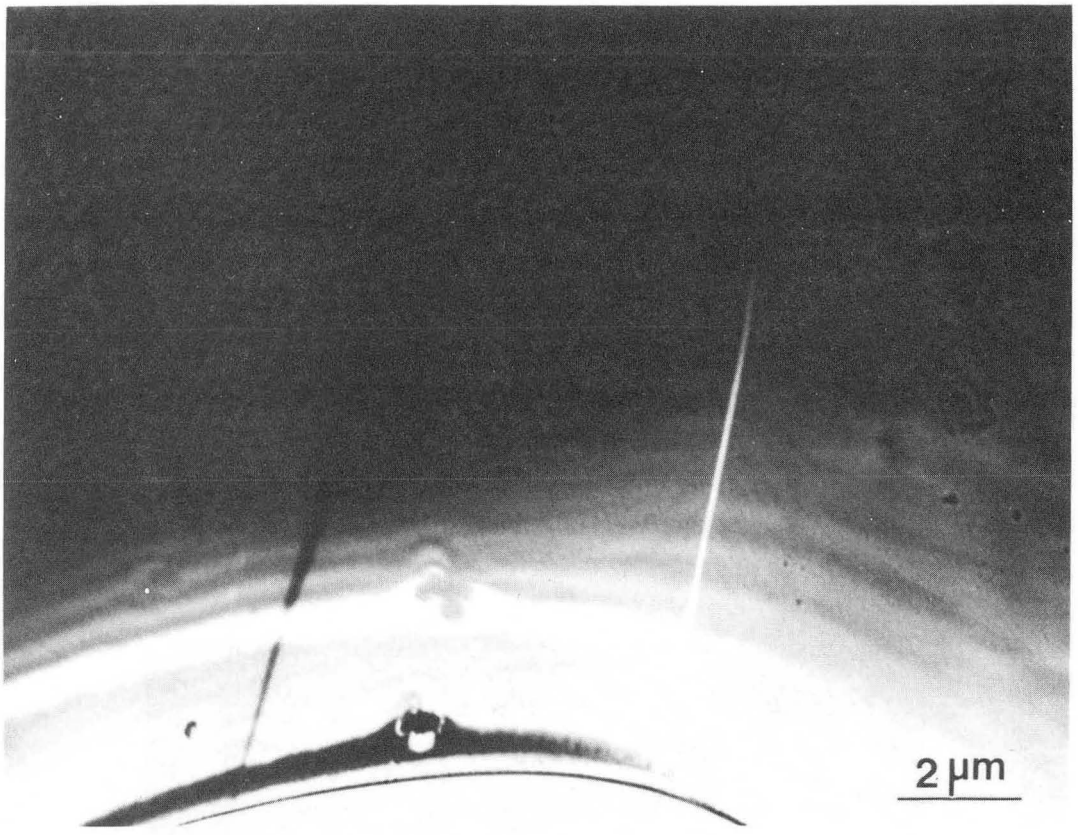

XBB880-10648

Figure 20

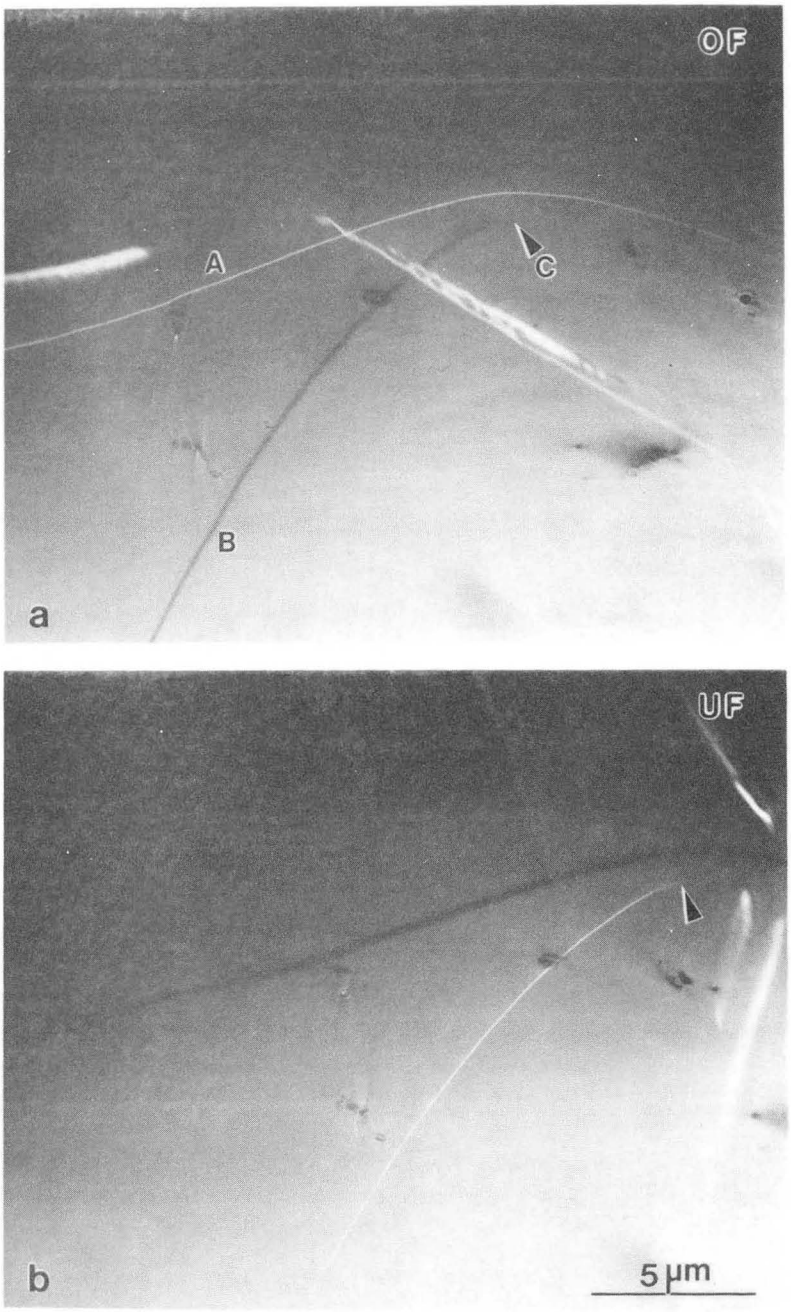

XBB889-8699-A

Figure 21

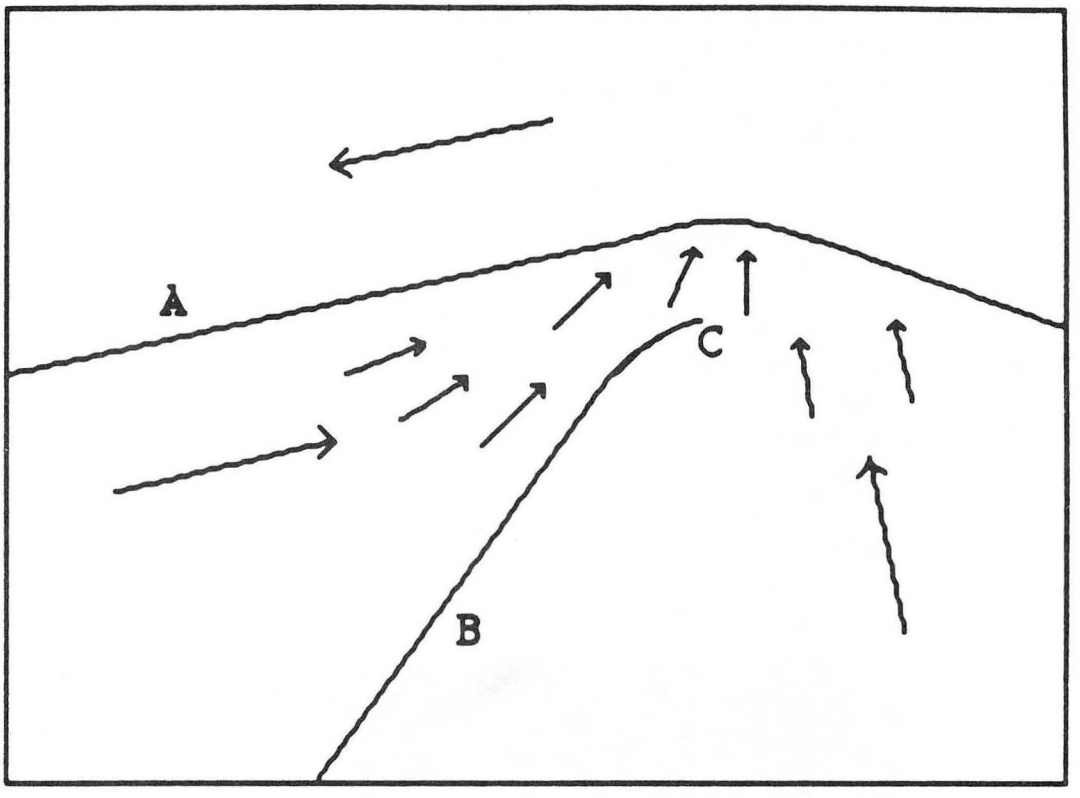

XBL 8811-3796

Figure 22

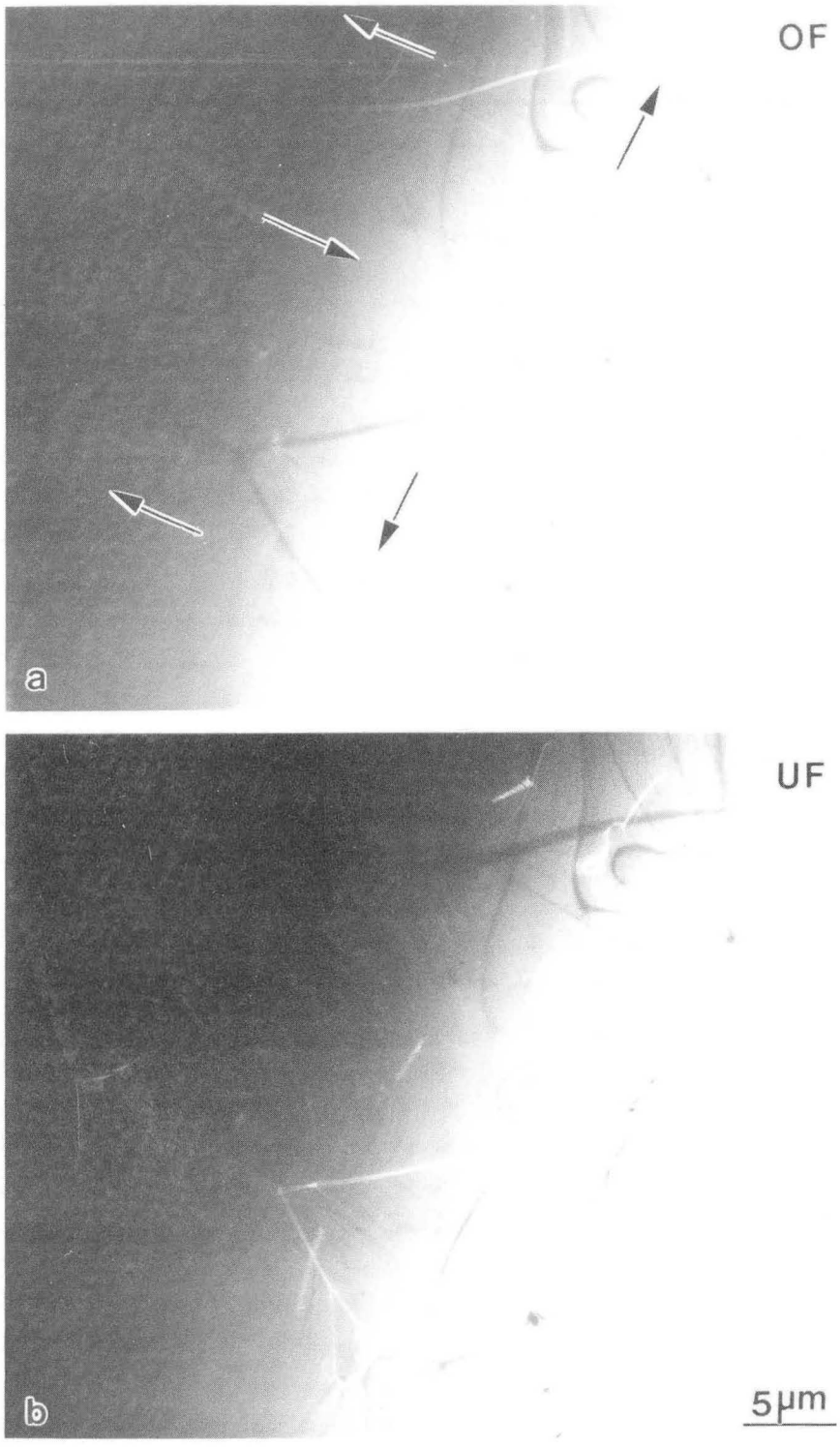

XBB889-8700-A

Figure 23

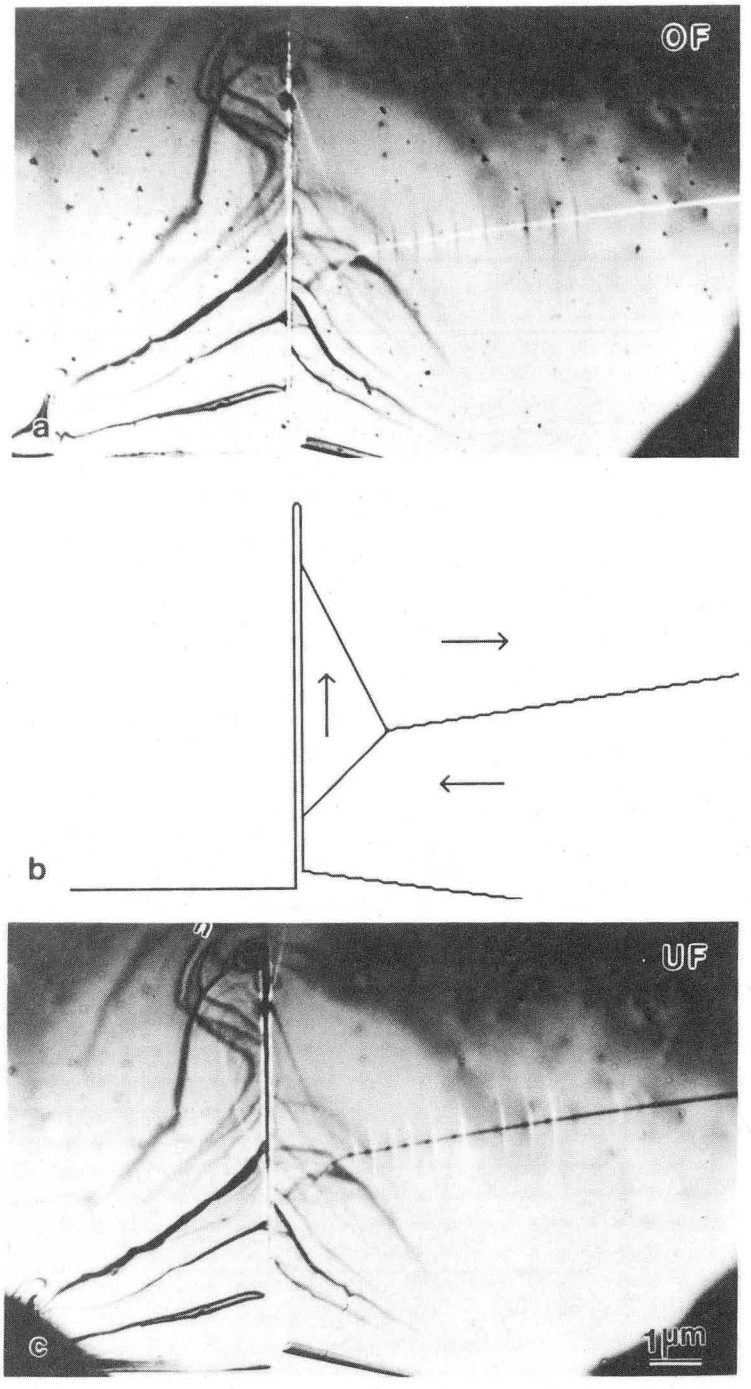

XBB889-8705-A

Figure 24

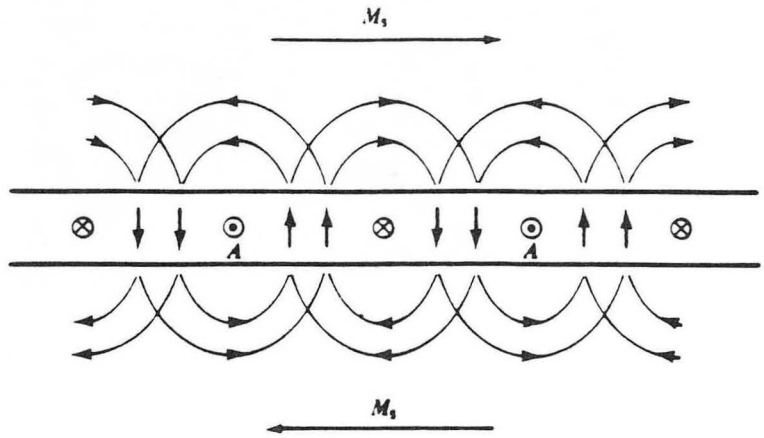

(a)

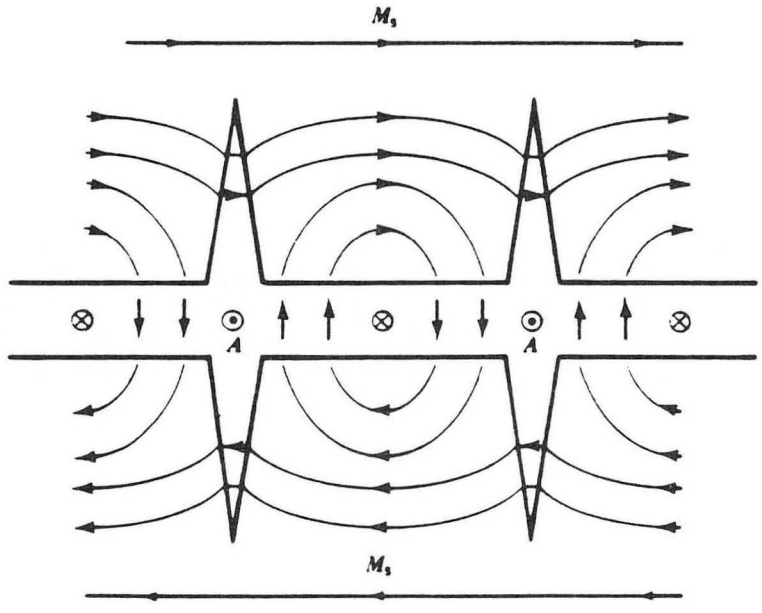

(b)

XBL 8811-3797

Figure 25

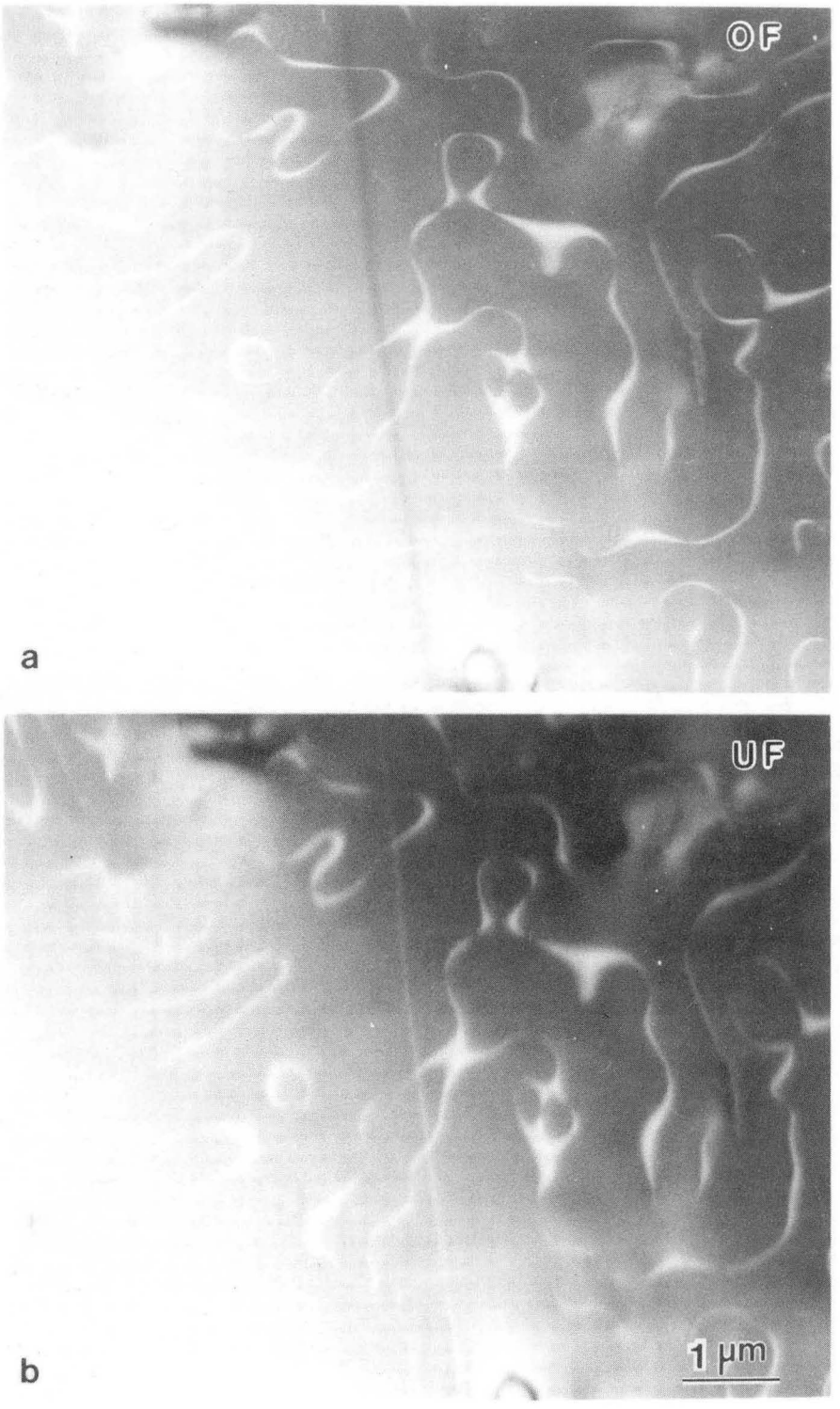

XBB889-8701-A

Figure 26

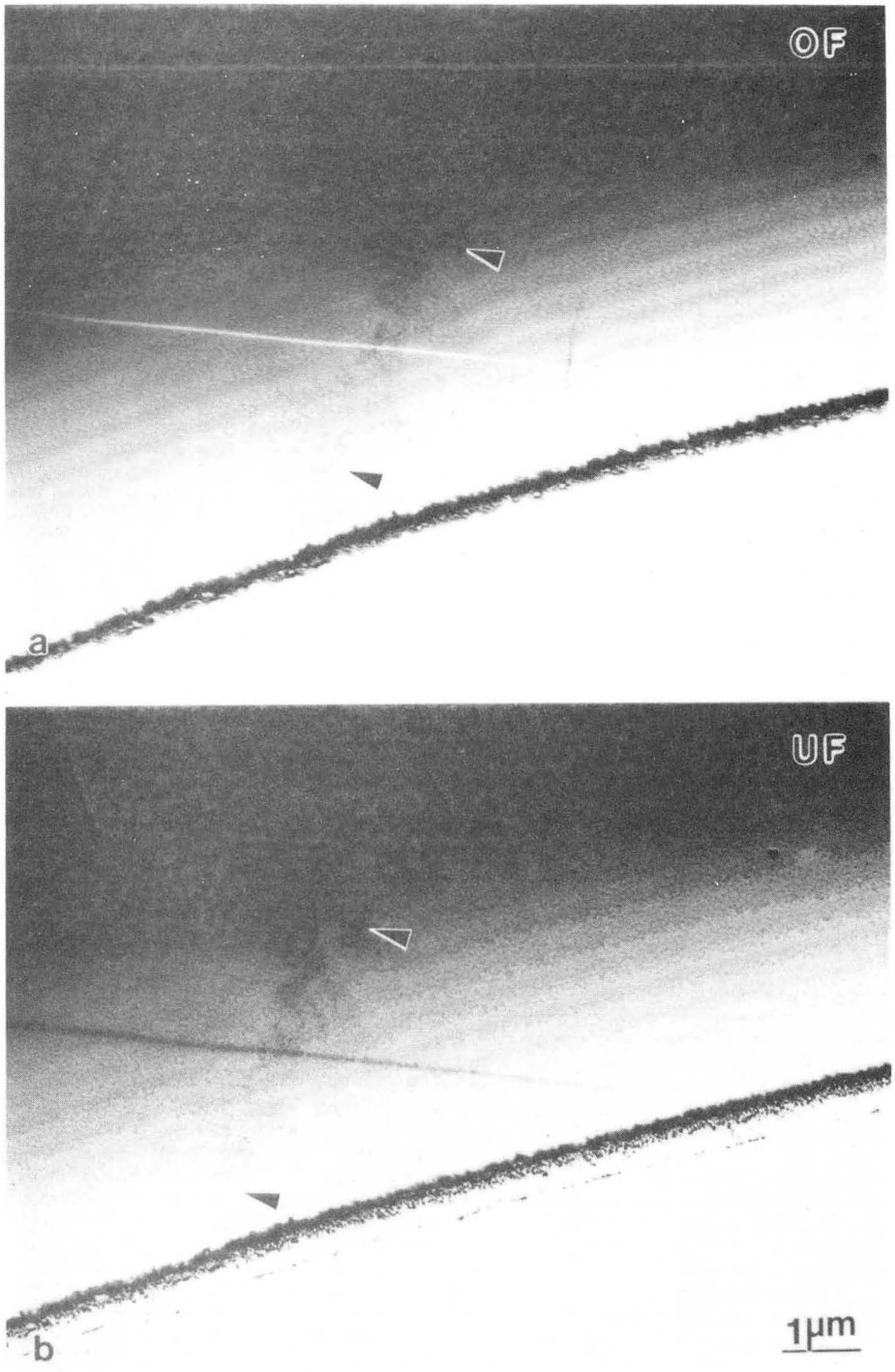

XBB889-8702A

Figure 27

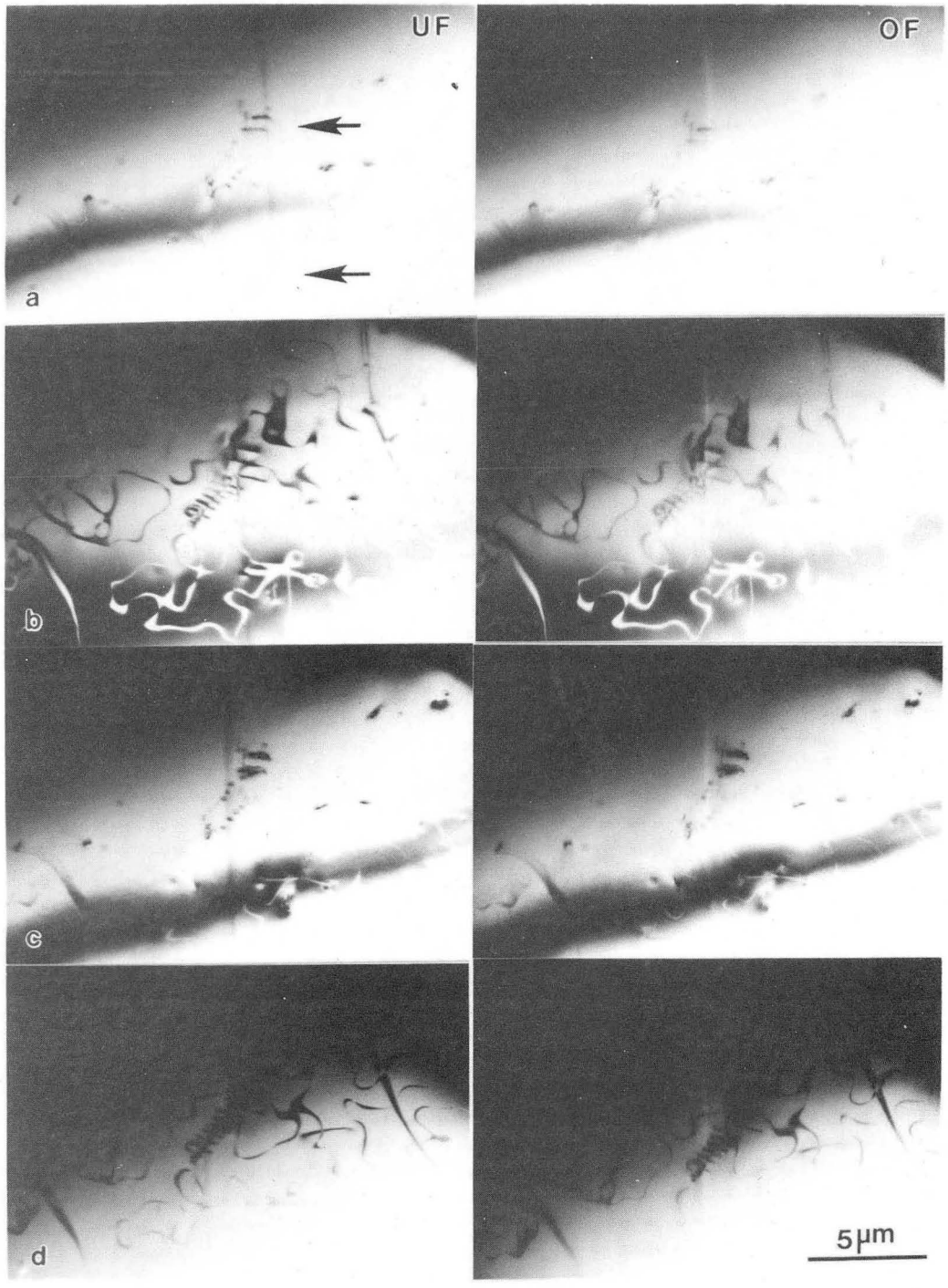

XBB885-5357A

Figure 28

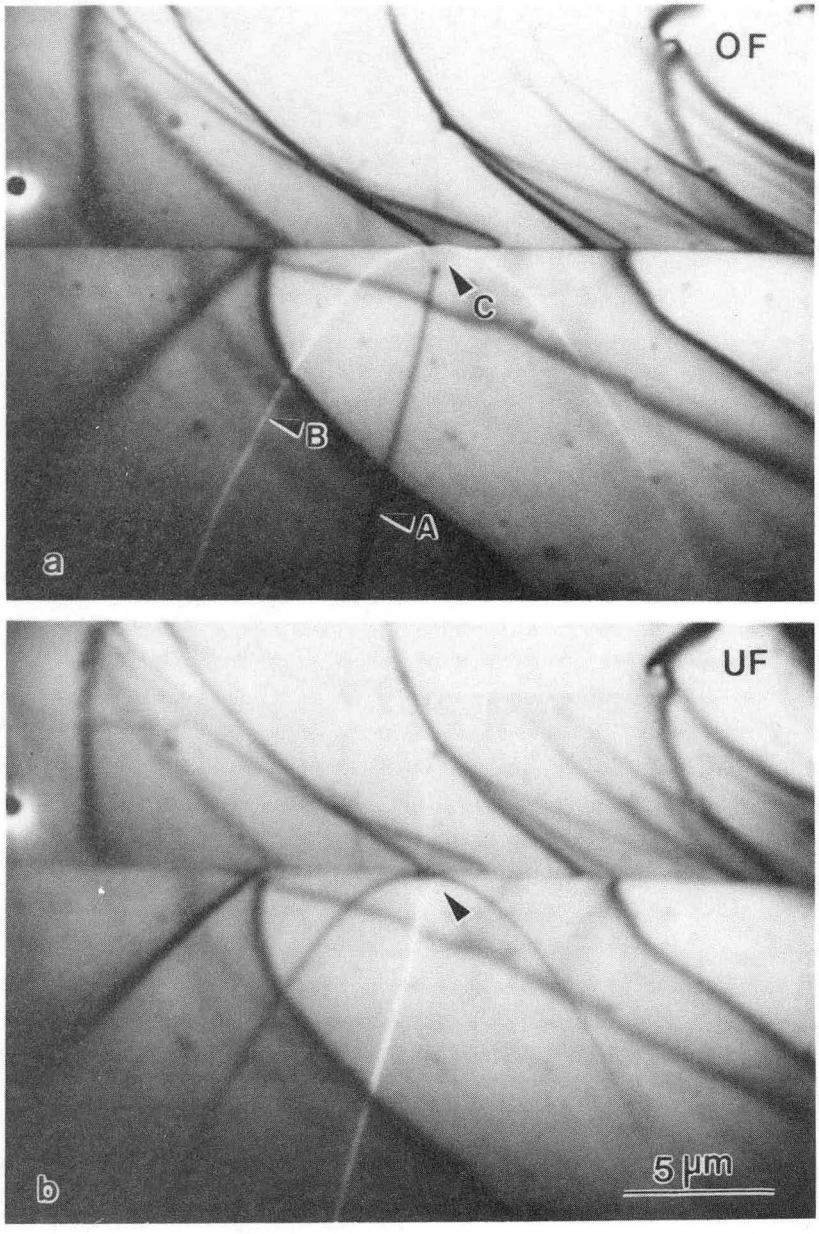

XBB 885-5241A

Figure 29

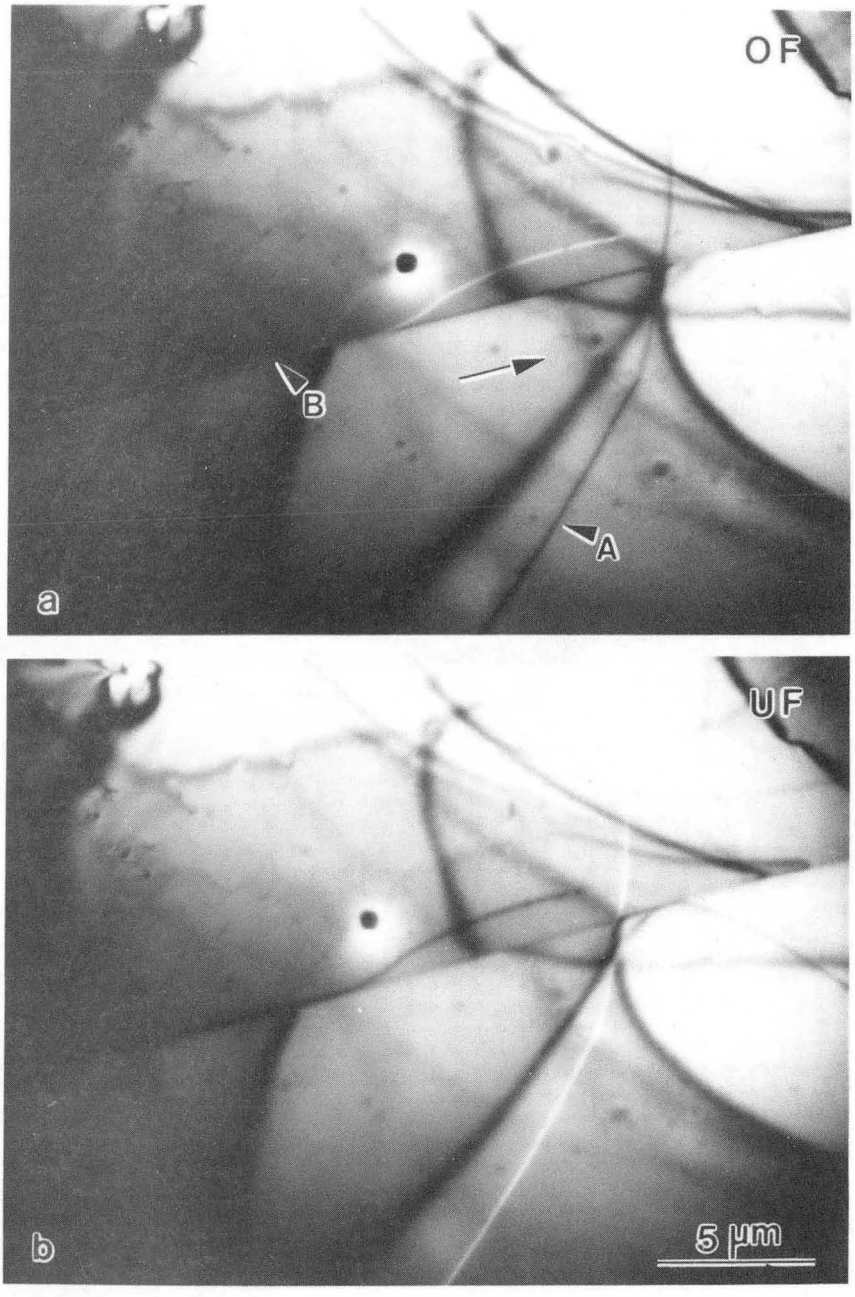

XBB885-5241B

Figure 30

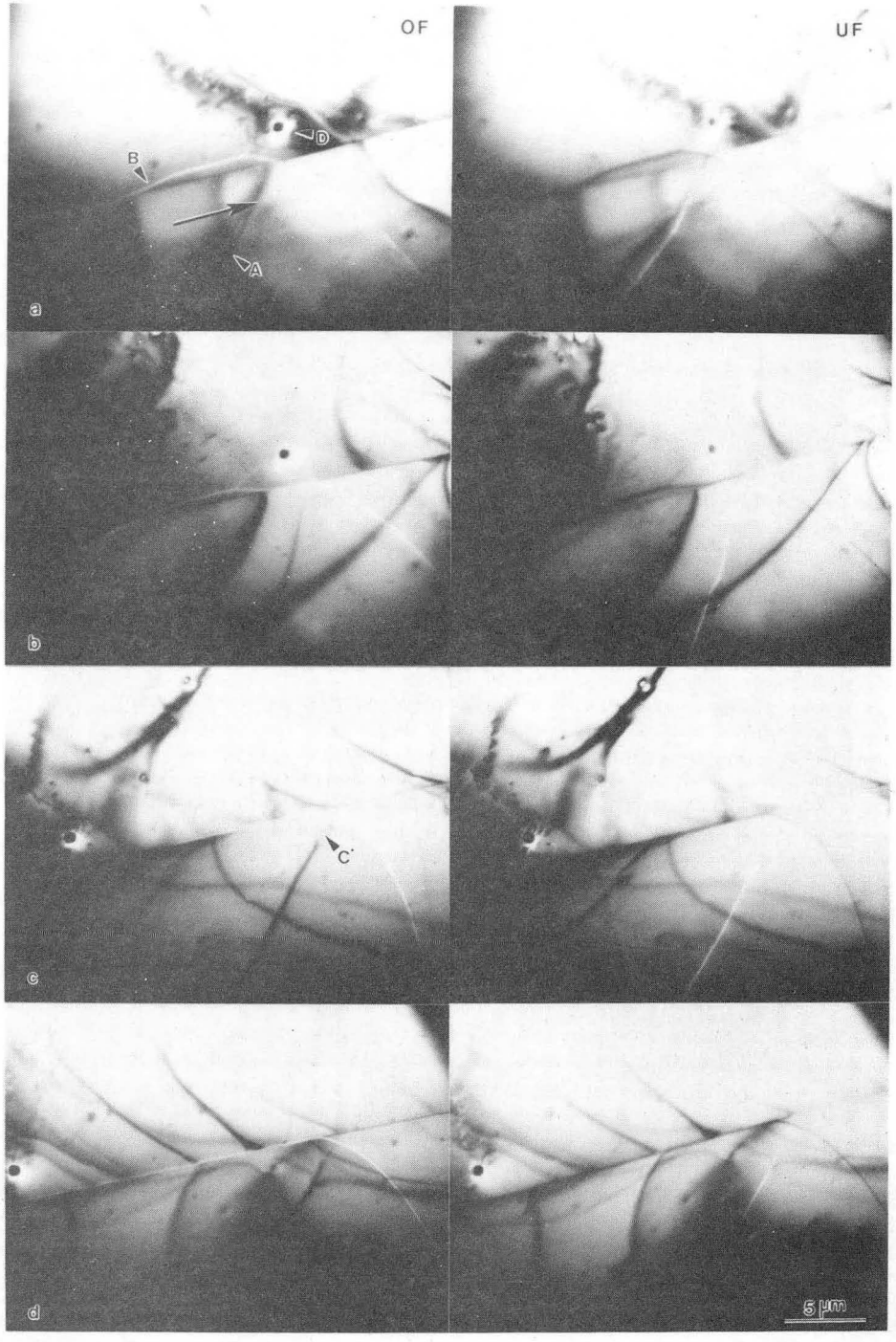

Figure 31

XBB885-5243A

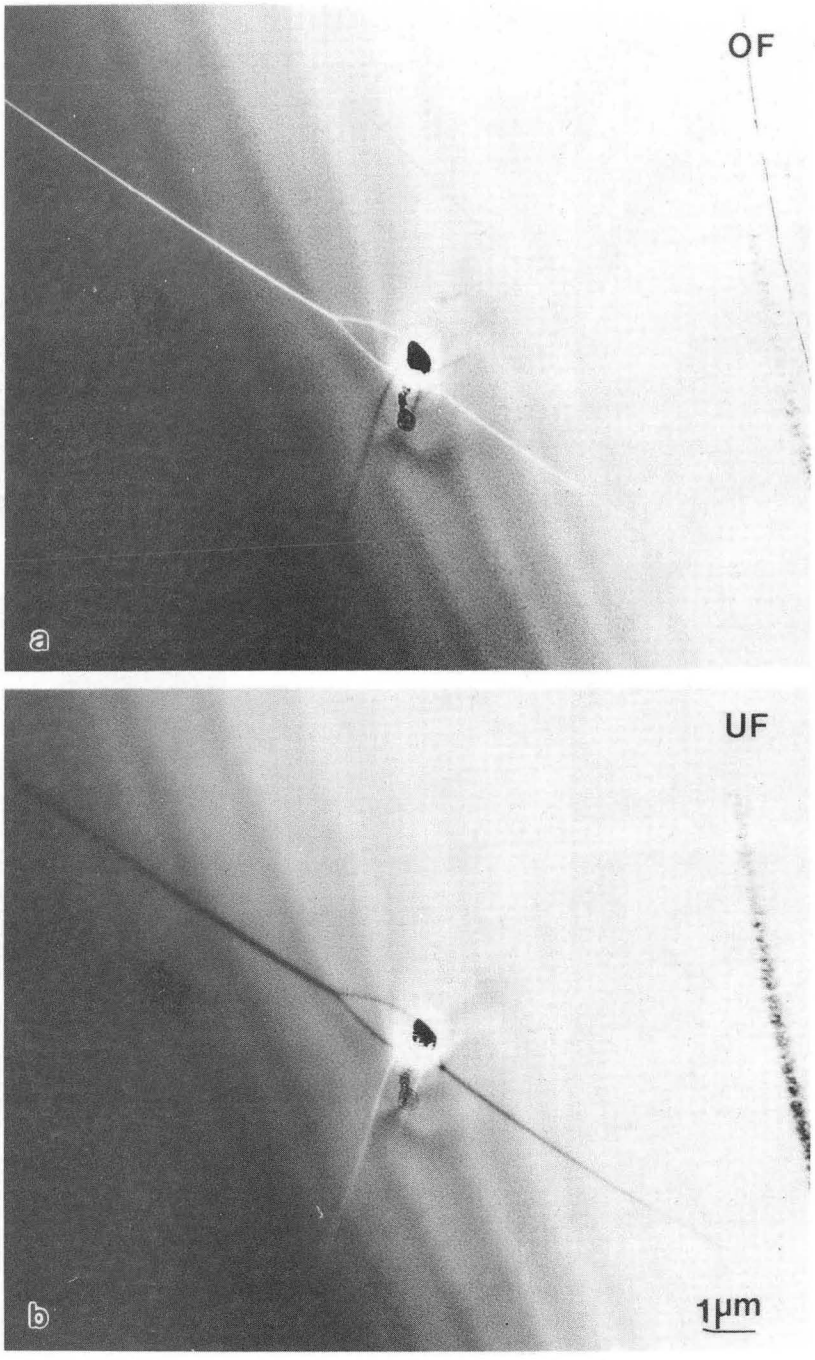

XBB889-8698A

Figure 32

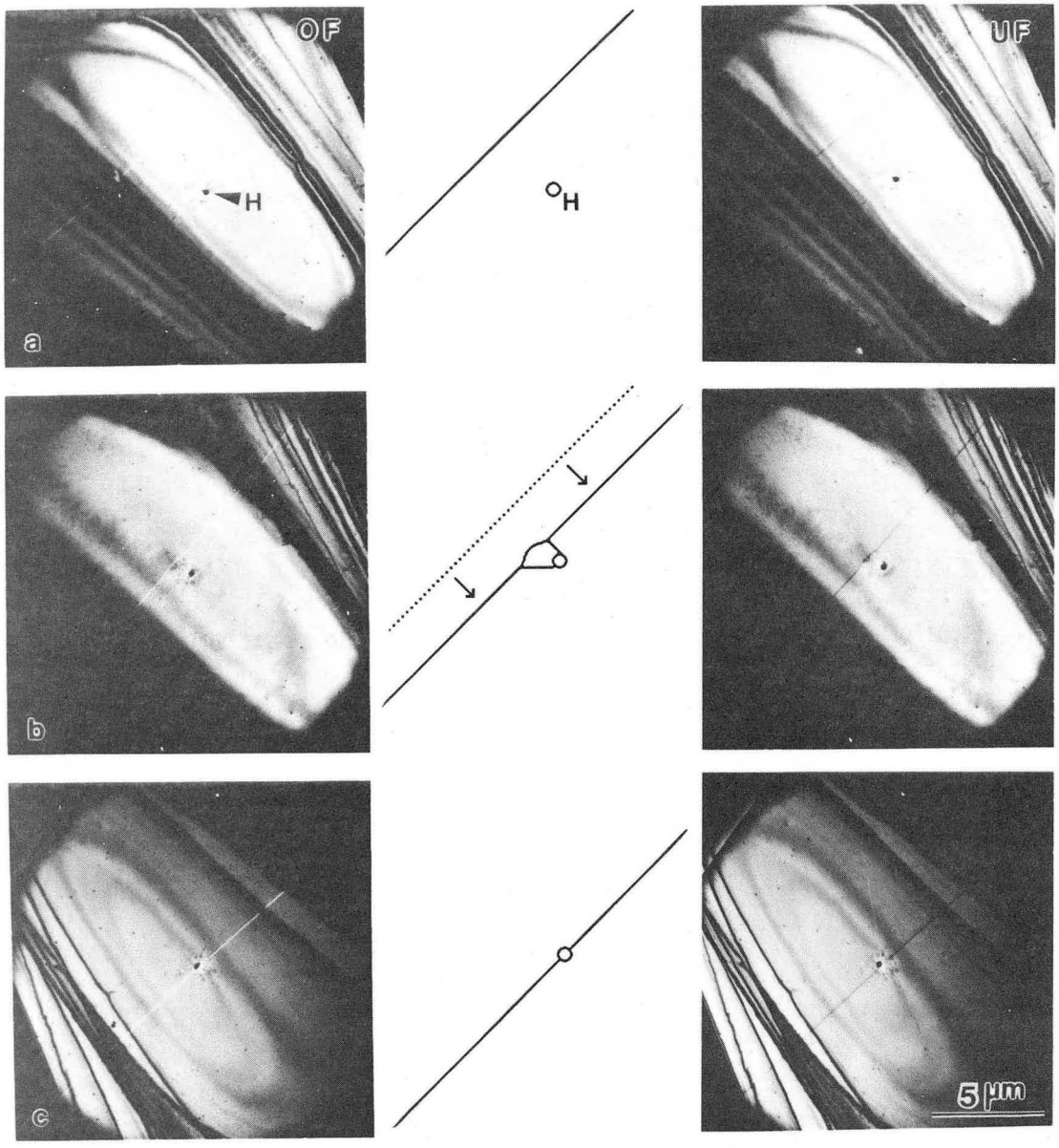

XBB889-8697A

Figure 33

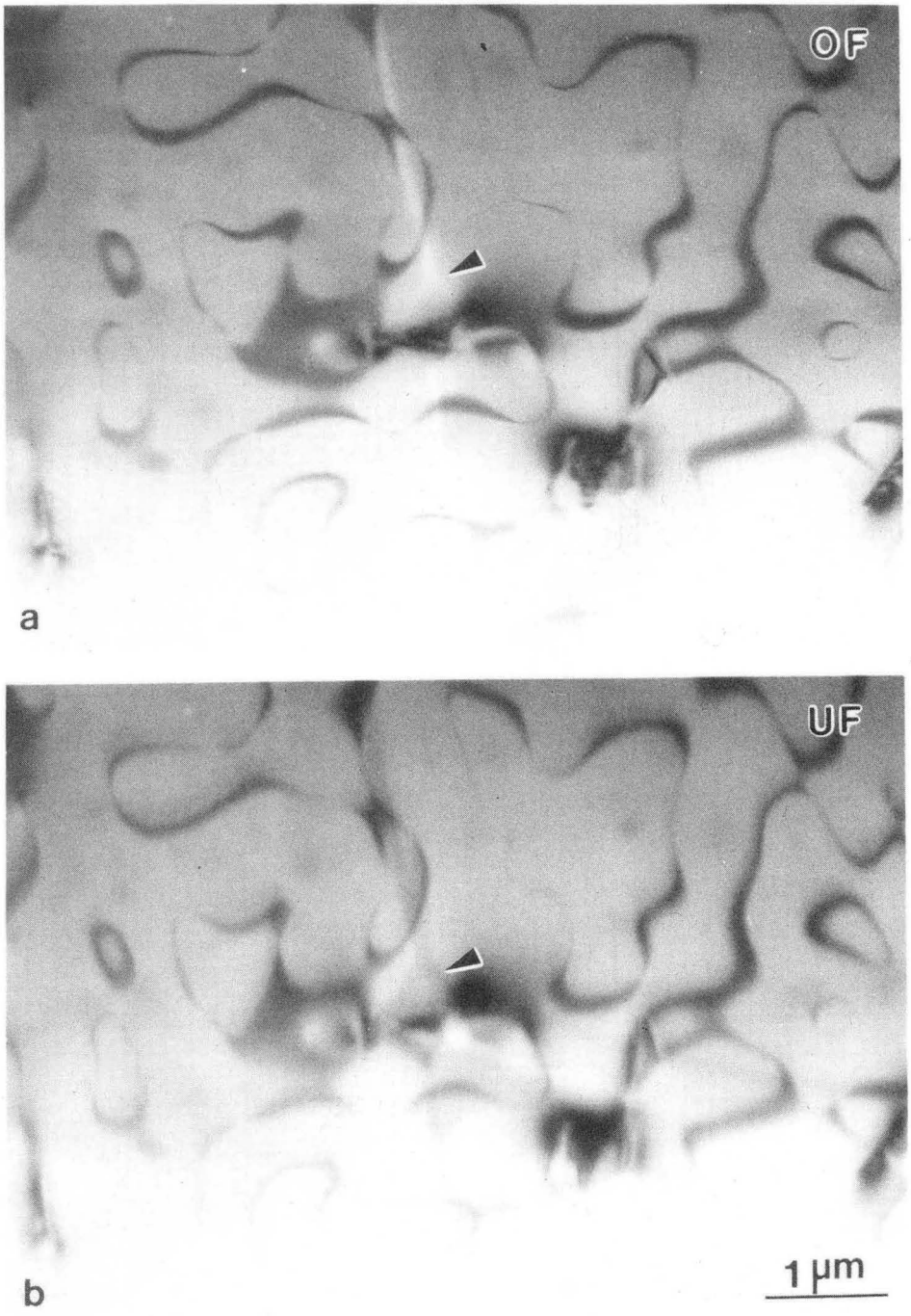

XBB889-8704A

Figure 34

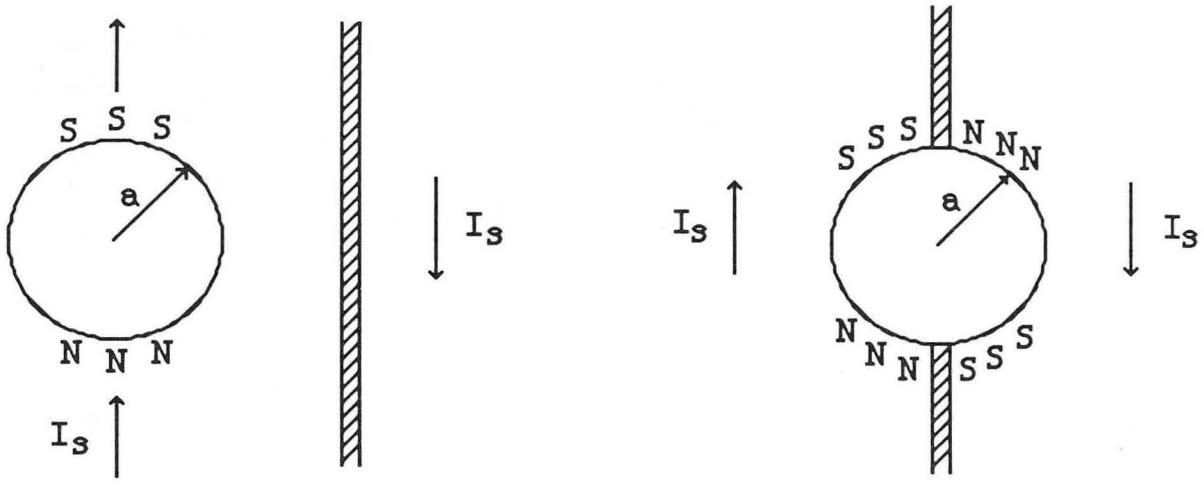

(a) (b)

XBL 8811-3798

Figure 35

LAWRENCE BERKELEY LABORATORY
TECHNICAL INFORMATION DEPARTMENT
1 CYCLOTRON ROAD
BERKELEY, CALIFORNIA 94720